1-1-2012

Correlation Of Printed Circuit Board Properties To Pad-Crater Defects Under Monotonic Spherical Bend

Brian Gray
Ryerson University

CORRELATION OF PRINTED CIRCUIT BOARD PROPERTIES TO PAD-CRATER DEFECTS

UNDER MONOTONIC SPHERICAL BEND

by

Brian Gray

Bachelor of Engineer Science, University of Western Ontario,

London, Ontario, Canada, 1996

A thesis

presented to Ryerson University

in partial fulfillment of the

requirements for the degree of

Master of Applied Science

in the Program of Mechanical Engineering.

Toronto, Ontario, Canada, 2012

AUTHOR'S DECLARATION FOR ELECTRONIC SUBMISSION OF A THESIS

I hereby declare that I am the sole author of this thesis. This is a true copy of the thesis, including any required final revisions, as accepted by my examiners.

I authorize Ryerson University to lend this thesis to other institutions or individuals for the purpose of scholarly research.

I further authorize Ryerson University to reproduce this thesis by photocopying or by other means, in total or in part, at the request of other institutions or individuals for the purpose of scholarly research.

I understand that my thesis may be made electronically available to the public.

Abstract

CORRELATION OF PRINTED CIRCUIT BOARD PROPERTIES TO PAD-CRATER

DEFECTS UNDER MONOTONIC SPHERICAL BEND

Brian Gray

Master of Applied Science

Mechanical Engineering

Ryerson University, 2012

The restriction of lead in solder has caused a change in base materials used to make electronics—the result of which has been a new failure mode known as pad-crater. The susceptibility of six commercially available printed circuit board (PCB) laminates to pad-crater by spherical bend test was determined. The correlation of PCB laminate tensile properties, Vicker's hardness (VH) of the resin, and weave dimensions showed an inverse relation between susceptibility to pad-crater and VH. Spherical bend testing of pure G10 laminate showed the orthotropic nature of laminates must be accounted for when modeling spherical bend. Comparison of bare PCB spherical bend test results showed the warp and weft direction have different strain responses for some materials. Comparison of strain energy of printed circuit board assemblies and bare PCB subjected to spherical bend showed the additional stiffness added by the ball grid array is almost identical for PCB laminates with different tensile properties.

Acknowledgements

Dedication

I dedicate this thesis to my life partner Marnie for her support and encouragement, and to our daughter Vivienne.

Table of Contents

List of Tables

List of figures

List of Acronyms

BGA – Ball Grid Array (electrical component)

CI – Confidence interval

CBB – Cold bump pull what

CDF – cumulative distribution function

CPB – Cold Pin Pull

Dk – dielectric constant

Df – dissipative factor

ICT – In-Circuit-Test

Gbps – giga bits per second

HBP – Hot bump pull

HPP – Hot pin pull

QFP – Quad-Flat-Pack

PCB – printed circuit board

PCBA – Printed Circuit Board Assembly

PDF – Probability distribution function

PPO – epoxy-polyphenelene

PPE – polyphenelene-ether

RRX – rank regression on x-axis

SAC – Lead free solder alloy made from Sn, Au, and Cu

SEM – scanning electron microscope

SLI – Second level interconnect

TBPPA – tetrabromobisphenol A

eV – electron volt

Nomenclature

e – Eulers constant, natural log base 2.71828

η – scale parameter, or characteristic life, for Weibull distribution

β – slope parameter for Weibull distribution

γ – delay parameter, or fail free time for Weibull distribution

ε – strain

P – load

ρ – correlation coefficient

δ – elongation

E – Young's Modulus

A – Area

T_g – Glass transition temperature

Q – stiffness

w – displacement of a plate

Chapter 1:   Introduction

The European Union restriction of hazardous substances (RoHS) outlined in Directive 2002/95/EC of the European Parliament restricts the use of lead (Pb) in solders to less than 1000 ppm [1]. This restriction has caused a shift in electronics assembly away from tin-lead (PbSn) eutectic solders to solders comprised of tin (Sn), silver (Au), and copper (Cu)–commonly referred to as SAC solder. The switch to SAC solders has had a far reaching effect across all aspects of electronics including reliability, quality, and base materials. The new SAC solders have a solidus temperature of 217°C and, as with non-eutectics alloys, they have mushy zones before becoming liquidus at temperatures ranging from 217°C to 227°C, depending on the alloy [2]. In comparison, PbSn eutectic solder melts at 183°C. PCB processing temperatures during reflow are typically 30°C to 40°C above the melting temperature of solder used to form solder joints. As such, processing temperatures for PCBs reach between 220°C to 230°C with SnPb solder, and 250°C to 260°C with SAC solder. The increased reflow temperatures associated with SAC solders has forced PCB manufacturers to change their epoxy resin formulations to increase cross linking thereby increasing material glass transition (T_g), and change curing agents from dicyandiamide (dicy) to phenolic novalec [3]. The increased reflow temperatures necessitate the addition of fillers (ceramic particles) to reduce out-of-plane coefficient of thermal expansion (CTE) of the PCB, thus reducing the stress on plated copper through vias [4]. Vias, which are copper plated holes in the PCB, are required to move electrical signal between layers of the PCB. The net effect of these changes is a harder and more brittle base resin material [5]. In comparison to

SnPb solder, SAC alloys in general have higher Young's modulus (E) and their Young's modulus increases with strain rate. Figure 1 shows the different failure modes of a BGA ball as per IPC/JEDEC 9702, Monotonic Bend Characterization of Board-Level Interconnect [6].
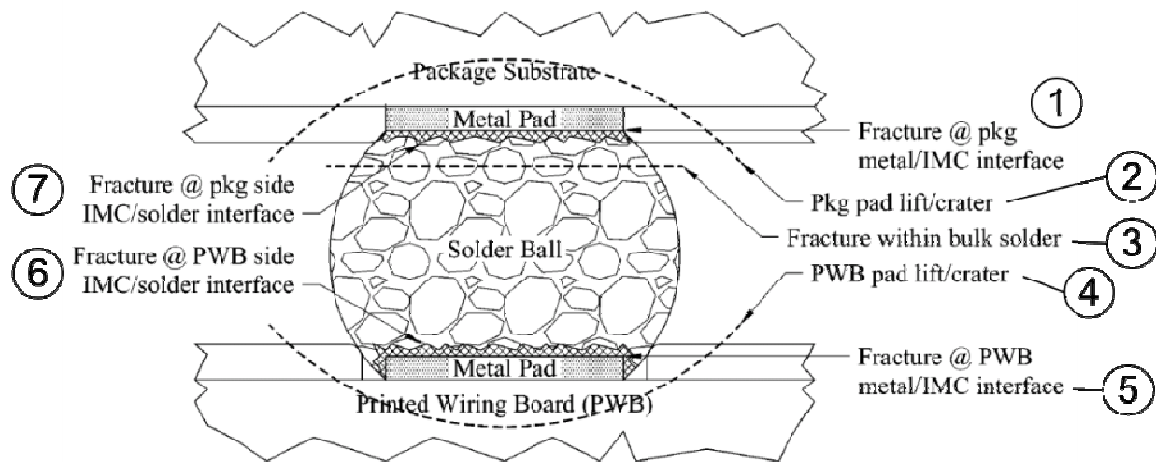
Figure 1: IPC9702 BGA Failure Mode Diagram [6]

With SnPb eutectic solder, the predominant failure mode of BGA solder joints were modes 6 and 7. With the introduction of lead-free SAC solder, the failure mode shifted to pad-crater–mode 4 as per Figure 1 [6]. An example cross section of a BGA pad-crater is shown in Figure 2.
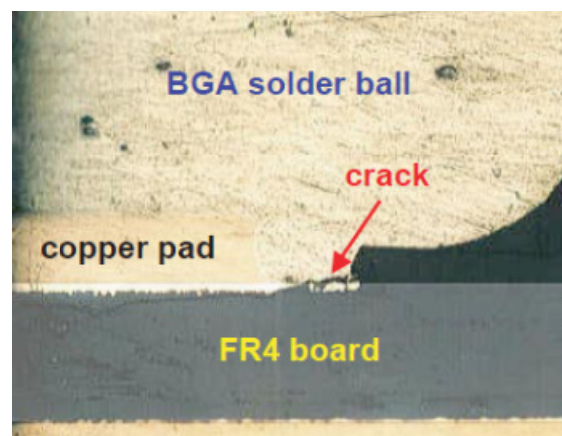
Figure 2: Example pad crater, 50 x magnification [6]

Pad-crater has no associated electrical failure unless it is catastrophic and occurs across many signal pads.

Pad-crater cracks have been shown to propagate slowly under thermal cycling; rather, the primary cause of crack propagation is isothermal stress [7]. If a pad-crater crack propagates across the signal pad, then all thermal and mechanical stresses will be borne by the copper signal trace. Due to copper's relatively low Young's modulus, this loading condition will almost certainly result in severing of the copper signal trace. If the crack propagates into the PCB, there is a risk of conductive anodic filament (CAF) growth between two copper features inside a PCB.

CAF is an electrochemical failure mechanism that occurs in the end-user environment which results in unintended electrical conductivity between two copper features in a PCB [8].
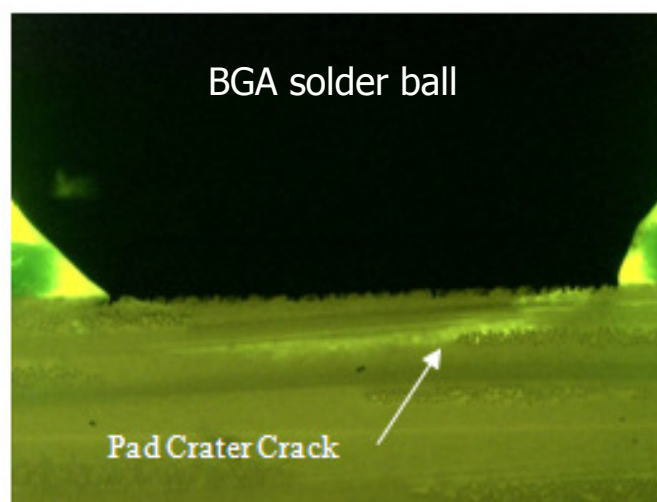
Figure 3: Pad Crater Crack Example, 100x magnification, fluorescing light [9]

For CAF to occur, three conditions must be present in a PCB: a crack between two copper features, moisture ingress into the crack, and voltage potential between the two copper features [7]. Multiple investigators have shown that pad-crater can travel below

3

the first layer of glass weave in a PCB [9,10] with one example shown in Figure 3. A crack as shown in Figure 3 in a PCBA with high density interconnects could easily occur between two copper features close to the PCB surface. A crack of this kind would provide a path for moisture ingress, making two of the three requirements for CAF present.

The deleterious effects of moisture ingress into a PCB can work to weaken the strength of the PCB in four different ways. Moisture present in resin of a PCB can replace the –OH bonds in the matrix, thereby breaking down the cross link bonds [11]. When water occupies free volume in the matrix, the molecules tend to coalesce which puts stress on the matrix [11]. The resin glass interface also breaks down in the presence of moisture [12] and cracks in the E-glass fiber are known to propagate faster in the presence of moisture [13].

Pad-crater mitigation techniques including dimensional changes to BGA corner pads and polyimide films between the signal pads and PCB have been investigated and have shown no appreciable increase in PCBA level surviving strain [9, 14]. Strain energy release rates (J_{ci}) for crack propagation of SAC solder and one lead-free PCB laminate showed J_{ci} rates to be higher for SAC solders [15,16]. Unless material changes are implemented to make J_{ci} values lower for solder than PCBs, thereby moving the failure point back to the solder where there is an associated electrical fail, pad-crater will prevail as the predominant mechanical failure mode.

1.1 Overview Printed Circuit Board Assembly (PCBA)

A PCBA is a PCB with attached application specific integrated circuits (ASIC), integrated circuits (ICs), resistors, capacitors and other electric components to make a finished electronics product. PCBAs are found in everything from cell phones to communication servers. In a cell phone, a PCBA may weigh roughly 100 grams and an internet backbone communication server PCBA can weigh over 15 kg with heat sinks attached. Regardless of size, a PCBA has a base PCB to which electrical components are attached with solder. A schematic of a PCBA is shown in Figure 4 complete with components typically attached.
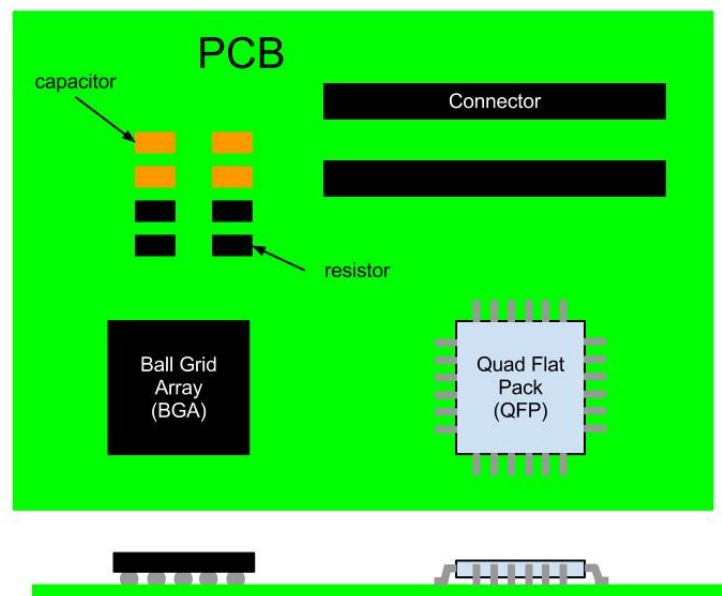
Figure 4: Printed Circuit Board Assembly

Assembly of a PCBA starts with a bare PCB. The PCB is screened with solder paste over the areas where solder joints are required. The solder paste is a mixture of small solder spheres, flux, and flux carriers. After screening, the PCB is populated with electronic components by pick and place equipment. Once all components are placed

5

on the PCB, it travels through an oven where it is subjected to a thermal profile that allows the flux carrier to evaporate, the flux to clean the surface to be soldered, and the solder spheres to become liquidus so they coalesce to form a solder joint. The solder joint serves as both a mechanical and electrical connection between the PCB and the component, and also provides a path for heat to dissipate away from the component.

1.2 Literature Review

There are no published studies that compare multiple PCB laminate material properties to their susceptibility to pad-crater when subject to monotonic spherical bend. Comparative spherical bend of different PCB laminates mounted with a ceramic ball grid array (CBGA) was shown to be an effective measure of a laminate's resistance to pad-crater, but no investigation into material properties was conducted [17]. Factors affecting a PCB laminate's susceptibility to pad-crater include thermal reflow history, exposure to moisture, PCBA construction, and temperature at the time of mechanical loading [10].

Investigations into pad-crater have primarily focused on correlation of joint level testing to PCBA level pad-crater, four-point bend testing, and pad-crater mitigation techniques. The principle of all joint level testing is to apply a load to a signal pad until failure. Joint level testing involves clamping the PCB at the edges with the test pad being the only point of applied load. Joint level testing can be divided into three categories: pin pull, bump pull, and shear. Figure 5 shows a schematic of all three test methods. Pin pull can be further divided into hot pin pull (HPP) and cold pin pull (CPP), and the test method involves attaching a copper pin to the test pad and pulling the pin

6

until pad failure. CPP occurs close to room temperature and HPP occurs at elevated temperatures to simulate end user conditions.
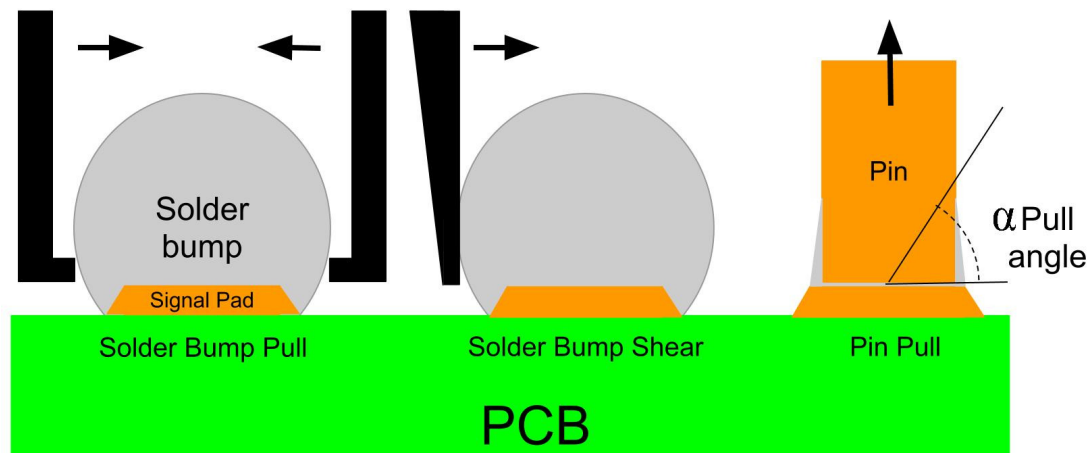
Figure 5: Bump Pull, Shear and Pin Pull

Bump pull can also be divided into hot and cold bump pull (HBP & CBP). Bump pull involves applying load through a solder sphere (bump) attached to the test pad. The bump is clamped by a special gripper that induces considerable deformation on the solder sphere, and then load is applied to the pad until failure. The large deformation induced by the grippers on the solder bump makes correlation of results to PCBA level pad-crater complex [18]. The pull angle for both pin and bump pull can be varied to simulate PCBA level loading, but one author has reported no difference in pad strength with change in pull angle, and another has reported an increase in cohesive pad crater over adhesive (see Figure 14) with decrease in pull angle from normal to the plane of the PCB surface [19, 20].

Shear testing applies a shear force with a blade to a solder bump and can drive failure in the PCB and the solder pad interface depending on the solder composition and PCB finish. Industry groups are using this method for correlation to pad-crater, but

7

their work is not published. Shear testing has been used to compare board finish and solder alloy's propensity for pad-crater during drop testing [21].

The advantages of joint level testing are that it is economical, repeatable, and results can be generated in short time. The drawbacks are that it cannot account for pre-stress that typically exist in PCBAs due to CTE mismatch between components and the PCB after assembly reflow. Furthermore, joint level testing provides the strength of a particular solder joint to a certain load that is directly applied to the solder joint. The results of such an assessment do not represent the actual end loading conditions found in a PCBA in the end user environment. In a real application, the loads are the remote boundary conditions of a PCBA, and these loads are transferred to the local area of the solder interconnects by PCB and/or modules on the PCB. As such, an investigation of the pad-crater failure must take into consideration the PCB behavior as well as the factors that determine the behavior. One study attempted to overcome these drawbacks of pad level testing by applying a constant bending load to a PCB before pin pull testing. The results of this showed that the peak load to failure decreased with increased board strain [22].

Four-point-bend testing in accordance with test method IPC/JEDEC 9702 [6] is a commonly used industry standard for comparatively testing PCB laminates under bend load. Figure 6 shows a diagram of a four-point-bend test with a test PCBA. The outer anvils are stationary while the inner anvils travel at a specified speed and displacement to apply load to the PCBA. The result is a constant unidirectional bending moment

applied to the PCBA between the inner anvils. Electrical continuity of the highlighted

solder joints in Figure 6 are monitored throughout the test to determine failing strain.
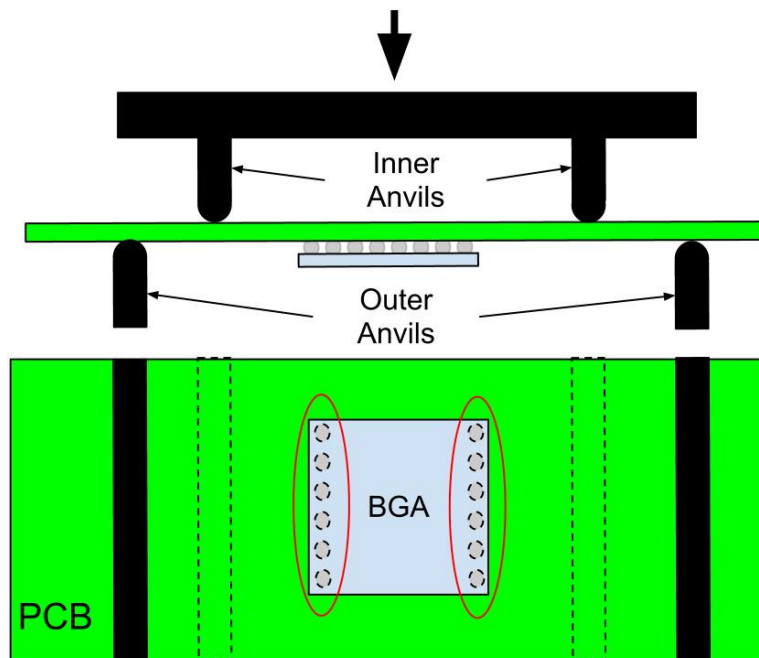
Figure 6: Four-point-bend test diagram

With PbSn solder, four-point-bend testing provides a comparative method for

determining the failing strain under constant unidirectional bend since the failure is in

the solder joint. With lead-free solders, where PCB laminate failure precedes electrical

failure, its shortcomings become apparent. The constant unidirectional bend moment

applied by the four-point-bend test is not typical of assembly or end-user conditions,

and the solder joints under test reinforce each other which over estimates the failing

strain.

In response to the shortcomings of joint level and four-point-bend testing, the

electronics industry developed the spherical bend test method [23]. This test,

performed at the PCBA level, is based on the ring-on-ring test method typically used on

glass and ceramics to find surface defects [24]. Spherical bend test method deforms a

PCBA into a hemispherical shape which applies a bi-directional bending moment to the corner solder joints. There is no reinforcement of the corner solder joints by neighbouring solder joints, and spherical bend is more representative of assembly and end user conditions. As such, spherical bend-testing provides the most accurate estimate of a PCB laminate's resistance to pad-crater defects.

Hsieh et al. [25] first published results of spherical bend in comparison to four-point-bend and concluded that spherical bend was a more conservative test method for pad-crater, and also more realistic test that simulated PCBA loading during in-circuit-test (ICT). The electronics industry traditionally used principal strain as the metric for determining process strain limits for PCBAs, but Lei et al. [26, 27] showed that principal strain as a metric for PCBA strain limits has a high degree of variation and is sensitive to bend mode. Principal strain is an indication of the maximum surface strain at the PCB surface, and does not necessarily correspond to the direction of maximum bend [26, 27]. Diagonal strain, or the strain coincident with the minimum bend radius for the spherical bend-test has been shown to have the best correlation to pad-crater defects, so it is the strain used for all analysis in this paper [27].

A SEM image of a test PCB laminate is shown in Figure 7 with the ceramic particles (fillers) highlighted. As the figure shows, the ceramic particles vary in size and are evenly spread throughout the resin. A SnPb eutectic PCB laminate would not have these ceramic particles due to the lower reflow temperature. Roggeman et al. [20] compared the crack path for filled and unfilled resin systems using hot bump pull and showed that for unfilled resin systems, the crack path travels into the PCB to the first

level of E-glass weave (see Figure 14) and for filled resin systems, the crack path is shallow and just below the copper (see Figure 14). Cyclic testing of the same PCB with hot pin pull showed filled resin systems to be 10 times more resistant to crack propagation [20].
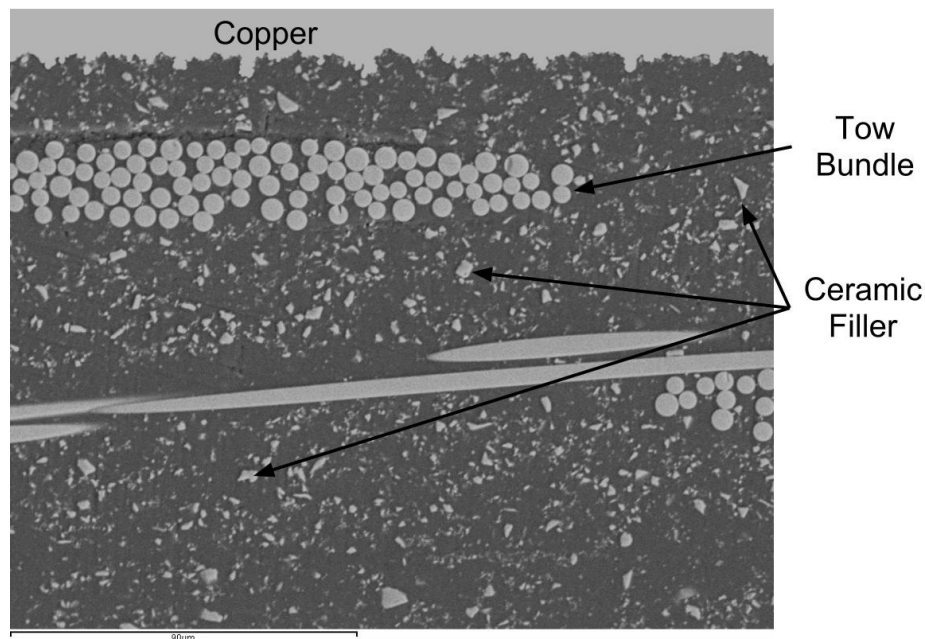
Figure 7: PCB Laminate G, SEM at 600x magnification, 10keV

A comparison of filled phenolic and unfilled dicy resins by hot pin pull showed the failing pin force for dicy cured epoxy to be about twice that of filled phenolic [19]. The addition of fillers to the phenolic resin and not dicy makes the comparison indirect, but it represents their end use condition.

Mukadam [7] et al. compared the micro-indentation hardness of PCBs as received and after three times reflow to 220°C and 260°C with results showing that micro-indentation hardness increased significantly with increased reflow temperature. Increased hardness does not necessarily translate into higher Young's modulus (E), but it suggests increased susceptibility to shear and flexural forces in the PCB [7].

11

CAF was first discovered as a failure mode in the 1970s during accelerated life testing, but was not widely reported until recently [28]. Increased processing temperatures exacerbate the CTE mismatch between the resin and the E-glass weave which puts more stress on the bond between E-glass and epoxy [8]. Pad-crater presents the opportunity for crack initiation point and combined with the weakened bond between the E-glass the epoxy matrix, one could logically conclude pad-crater increases the risk of CAF.

1.3 Objectives of Thesis

Pad-crater defects are a localized failure phenomenon that is affected by both local and global parameters of the PCBA structure and its constituent material properties. The literature review showed that there are no published studies relating PCB material properties to their susceptibility to pad-crater at the PCBA level. Instead, the electronics industry has chosen to primarily perform joint level and four-point-bend testing, and correlate the results to PCBA level pad-crater despite their shortcomings. A correlation between PCB laminates' resistance to pad-crater and its material properties would provide a better understanding of which material properties should be controlled to minimize pad-crater.

Finite element modeling of PCBAs with solder as the point of failure afforded simplifications in the PCB model since it was not the region of interest. With the failure moving from the solder joint into the PCB, accurate modeling of PCB behaviour is a prerequisite for modeling pad-crater failure. Due to the short time the spherical bend test has been employed, there have been no published investigations into the effect of

altering the boundary conditions of spherical bend, or the strain energy for PCBAs versus bare PCBs. Bend testing of pure laminate and two different bare PCBs at two different spherical bend boundary conditions is presented. Also, strain energy of two different PCBAs in comparison to bare PCBs is presented.

1.4 Overview of Thesis

Chapter 2 presents an explanation PCB manufacturing processes, base materials and properties used to make PCBs, BGA test component, and a detailed explanation of the pad-crater defect. In chapter 3, the details of the PCB stack-up, BGA test component, and assembly process are presented. Test methods to be used including PCB laminate tensile properties, Vicker's Hardness, spherical bend test, strain measurement, and bend test methodology are also presented in Chapter 3. A summary of all test results and analysis is presented in Chapter 4. Finally, conclusions are presented in Chapter 5.

Chapter 2: Constituent Materials of Printed Circuit Board Assembly (PCBA)

2.1 Printed Circuit Board (PCB)

PCBs are a composite material comprised of cotton paper or E-glass reinforcement with resin providing the matrix material. Copper is also present in the form of signal traces and power/ground planes. In layers of the PCB that carry signals, there is a limited amount of copper because the traces are narrow and can be ignored at a macroscopic level.
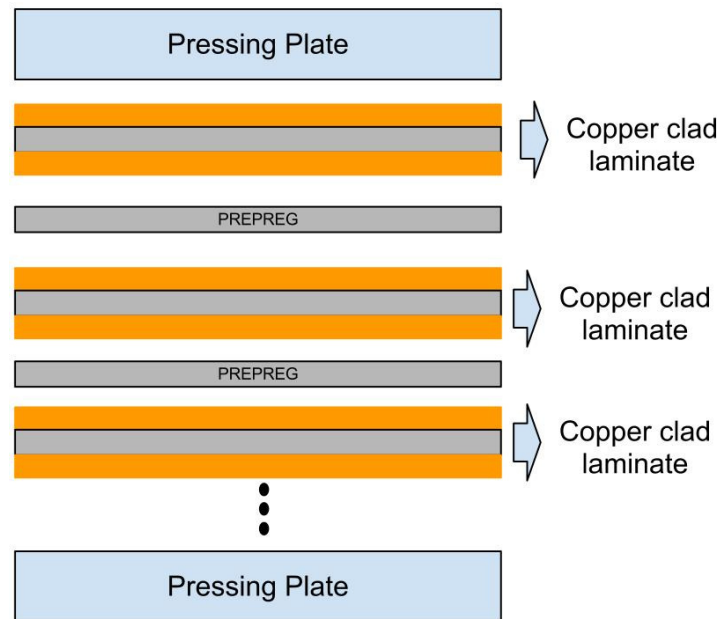
Figure 8: PCB pressing process

In layers with power and ground planes, copper can often occupy 80% or more of the layer so for modeling and theoretical analysis, the effect of the copper must be considered. This paper investigates pad-crater in PCBs made from lead-free compatible PCB laminates and E-glass weave with ceramic particles.

PCBs are manufactured by combining layers of E-glass weave, resin and plated copper, and pressing them together in the presence of heat as shown in Figure 8. The heat promotes cross linking and flow of the resin.

14

2.1.1 Resin Systems

The transition from PbSn eutectic solders caused a change from dicy cured epoxies because they cannot survive the higher processing temperatures of SAC solders, and their susceptibility to water absorption [29, 30]. Increased sensitivity to water absorption is driven by the increased water vapour pressure between SnPb and SAC processing temperatures.
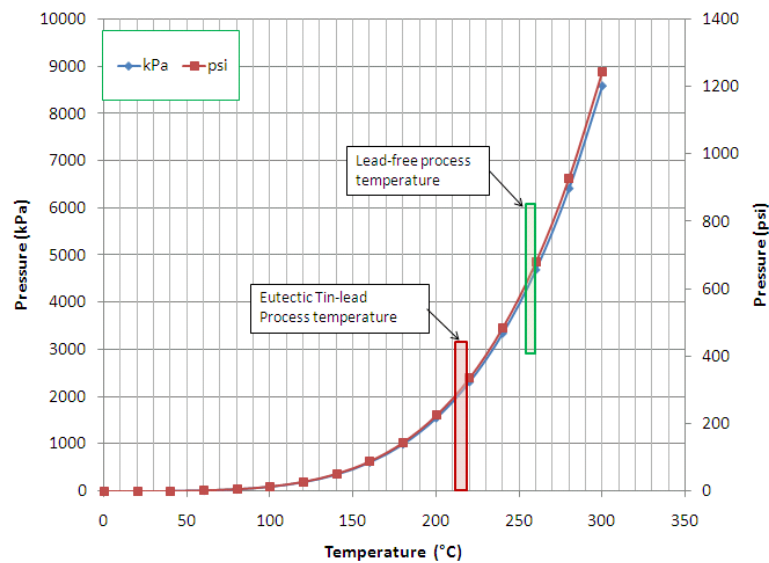
Figure 9: Water Vapour Pressure vs. Temperature

Figure 9 shows water vapour pressure vs. temperature with SnPb and SAC processing temperatures highlighted [31]. The near doubling of water vapour pressure can cause internal damage to the PCB such as delamination with dicy cured epoxies.

Resins compliant with SAC reflow temperatures have more cross linking which increases their glass transition temperature (T_g) reducing the overall CTE. While increased cross-linking produces stronger resins, they are also more brittle, which likely contributes to their susceptibility to pad-crater [30]. Further reduction of the CTE is

accomplished by the addition of ceramic particles [32]. Examples of SAC compliant resins are tetrafunctional epoxy, phenol novalec, epoxy-polyphenelene (PPO), polyphenelene-ether (PPE), among others. Figure 10 shows the molecular structure for tetrafunctional and phenol novalec resins.
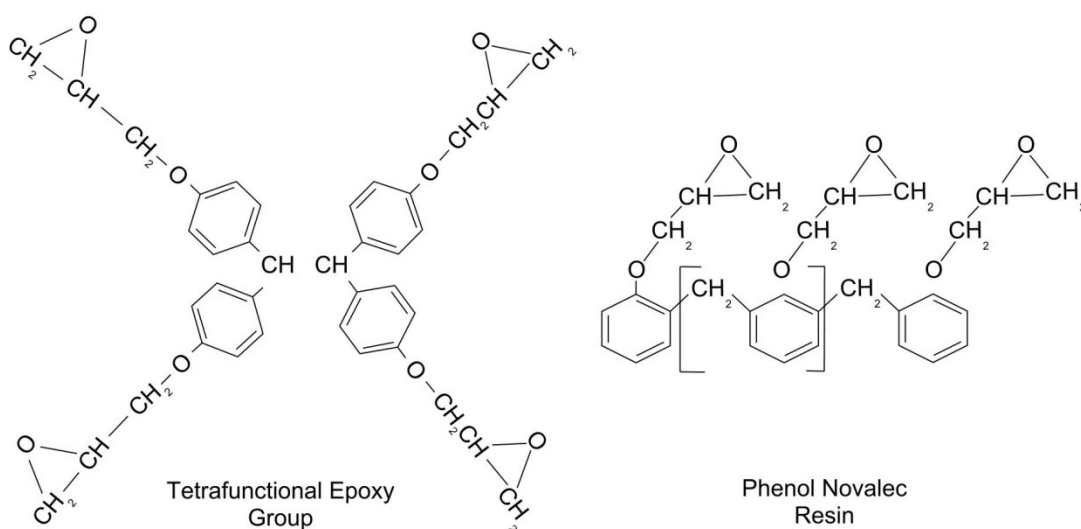
Figure 10: Tetrafunctional and Phenol Novalec Resin molecular structure [33]

Phenol novalec and tetrafunctional based resins have dielectric constant (Dk) and dissipative factor (Df) properties that make them suitable for lower frequency applications, and have T_g ranging from 125°C to 190°C [34]. The test PCB laminates that fall into this category have T_g equal to 170°C.

PPO and PPE are low loss materials and are used for higher frequency applications where transmission rates exceed 3 giga bits per second (Gbps) [35]. The test PCB laminates that fall into this category have T_g values ranging from 210°C to 215°C.

Brominating epoxy resins has been the typical path to the necessary flame retardancy in PCBs [36]. One common path to incorporating bromine into the resin structure is to use halogen containing tetrabromobisphenol A (TBPPA) [36]. RoHS

legislation does not currently restrict TBPPA, but the anticipation of a restriction has caused the development of halogen-free PCBs. A phosphorus based halogen-free PCB laminate was therefore included.

2.1.2 E-Glass Fabric Weave

A tow is an untwisted collection of fibers which, when arranged in a pattern, forms a fabric. For PCBs, the E-glass material is a plain weave fabric and as a fabric, it has two directions known as warp and fill.

1080 weave   2116 weave   7628 weave
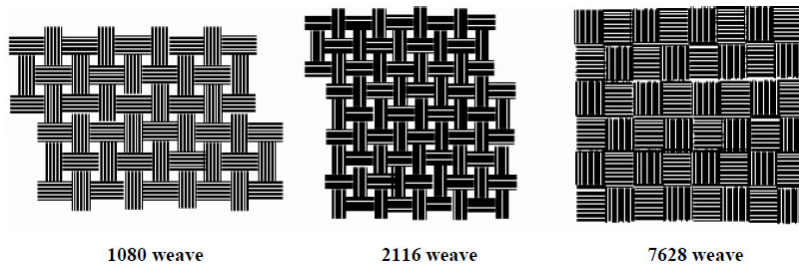
Figure 11: Plain Weave Fabric Types as per IPC4611A   [37]

The warp direction is the direction in which every second tow is oscillated up and down while fiber tows are inserted or filled into the fabric. Since in the warp direction tows are moved up and down during the manufacturing process, they tend to oscillate more than the fill tows. This can lead to slightly different properties depending on material direction. Figure 11 shows three examples of E-Glass fabric typically used in PCBAs. E-glass weaves are constructed in accordance with IPC4412A in terms of glass content and number of weaves per unit length in the warp and fill direction.

There are many considerations for selecting the base material for a PCB; electrical performance and reliability ultimately drive material selection. Multiple layers of E-glass weave between signal layers are often used to reduce the risk of CAF and weave processes used to construct the fabric can affect the Dk and Df properties. The fiber

17

weave effect (FWE) is a factor which affects digital signal transmission over 3 Gbps and it is directly affected by the non-homogenous nature of E-Glass weave [38]. E-glass weave can be processed to make the glass more evenly spread which reduces its non-homogeneity and reduces FWE [38]. Two additional benefits of spread glass are increased area for resin to bond to the E-glass and more continuous material properties at a microscopic level [38]. Vendors may or may not twist the bundles of E-glass for manufacturability which can greatly affect the microscopic properties of the PCB [39]. Bonding of the organic resin system to the inorganic E-glass weave is typically achieved with an organosilane compound which aids in wetting [40].

2.2 Solder, Copper, PCB and G10 Properties

Published values of Young's modulus (E) for SAC solders range from 45.9 GPa to 46.5 GPa [41, 42] and for SnPb eutectic solder E values range from 38.5 to 39.2 GPa at room temperature [43]. Both SAC and SnPb eutectic have increasing E with strain rate, although the effect is more pronounced with SnPb solders [44].

Published bulk copper properties for E is 128.7 GPa [45]. The copper that is present in a PCB has been electroplated and investigation of this type of copper's E value has ranged from 88-112 GPa with the average being 100 GPa–the value used throughout this paper [46].

The E values for all PCB and G10 laminate calculations are the average value from the tensile testing. The poisson ratio (v) for both PCB and G10 calculations is 0.34 [47].

18

2.3 Ball Grid Array (BGA) Component

A BGA is an electronics package used to attach an ASIC to a PCB.
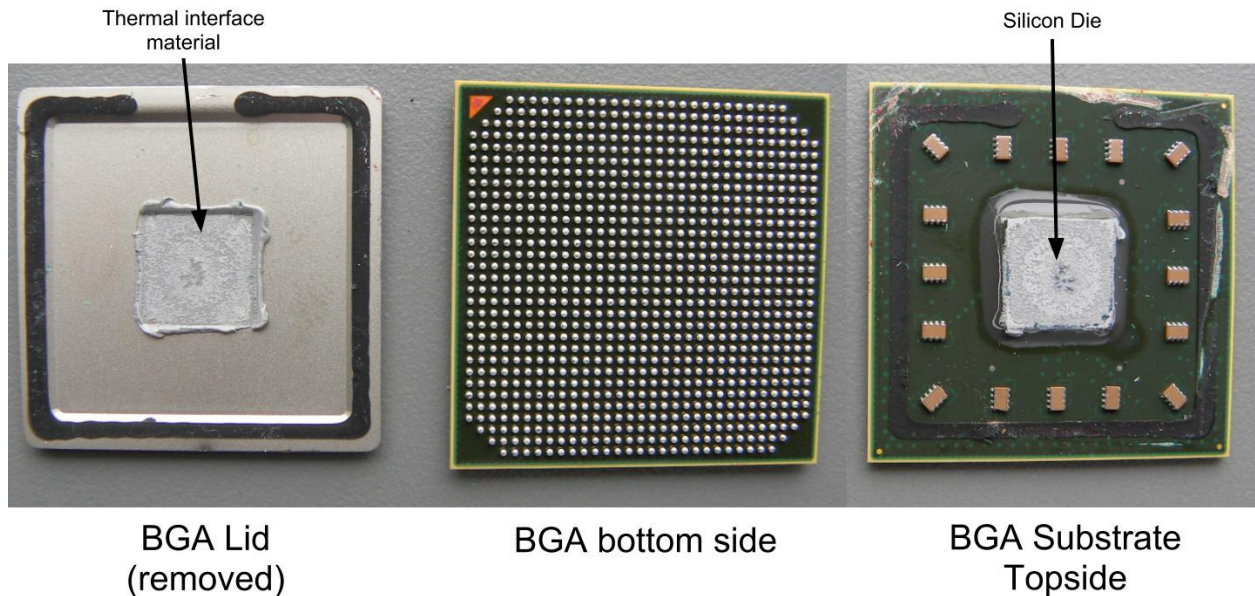
Figure 12: Ball Grid Array Package with lid removed

The BGA is essentially a miniature circuit board with a silicon die attached to one side and a high density array of second level interconnects (SLI) in the shape of solder spheres on the other. Figure 12 shows the bottom side, detached BGA lid, and top side of the test BGA. The BGA is 31 x 31 mm^2 with a pin count of 937. The copper lid in Figure 12 shows the thermal interface material in the middle and the black adhesive used to attach the lid to the BGA substrate around the edges. The BGA provides the highest density of solder connects per unit area.   Its drawbacks are that it lacks the compliance provided by a package with gull wing leads such as a Quad Flat Pack (QFP), and the BGA provides no opportunity to repair solder defects so it must be completely removed in the event of a process defect. A cross-section of the PCB with the attached BGA is shown in Figure 13.
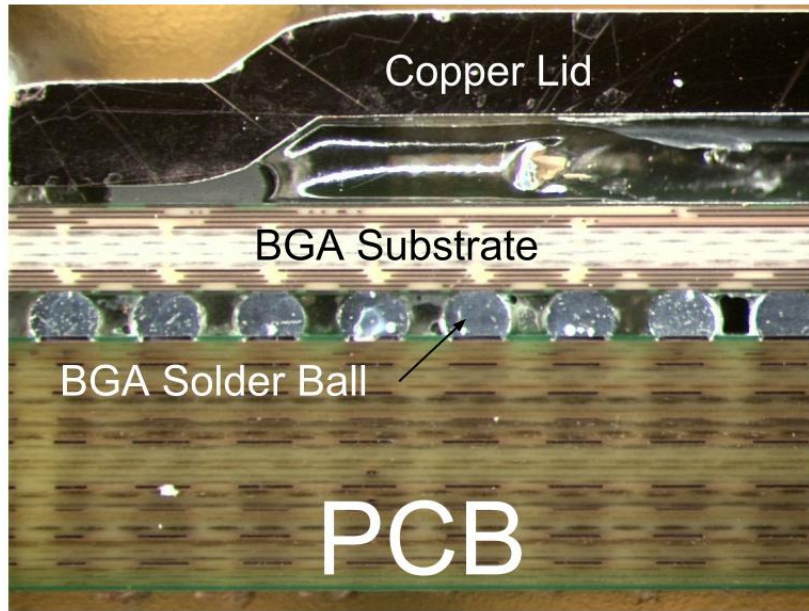
Figure 13: Attached BGA Cross section, 20x magnification

2.4 Pad-Crater

This paper defines two crack propagation paths for pad-crater. One crack path is directly below the signal pad and is considered to be an adhesive failure of the resin to the copper signal pad. The second crack path travels from the edge of the signal pad down through the resin layer to the first layer of fiber glass weave. This crack path is initially a cohesive failure of the resin and then becomes an adhesive failure of the resin to the E-glass weave. Both crack paths are shown in Figure 14. Some do not consider the adhesive failure to be pad-crater [7], but from a reliability perspective either crack path presents a risk to an electronic product's long term reliability.
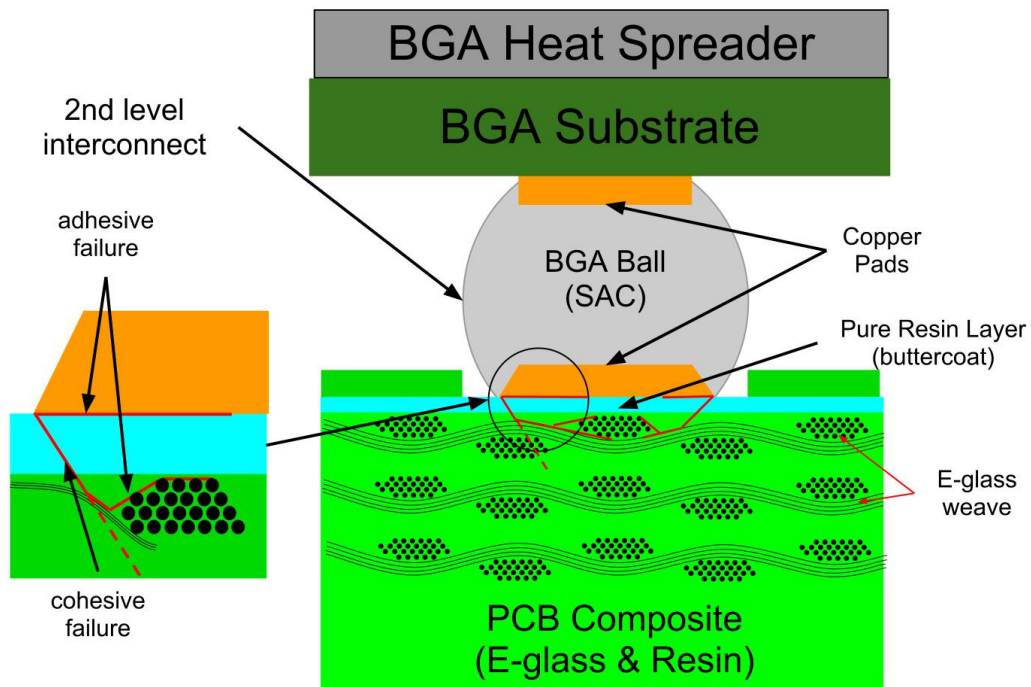
Figure 14: Pad-crater crack paths

As observed by others, the initiation of a pad-crater crack happens well before any electrical connection is broken so it is possible to ship electronics products to the field with latent defects [7, 9, 10, 14].

Chapter 3: Printed Circuit Board Assembly (PCBA), Bend Testing, and PCB Laminate Properties and Characteristics

The PCB base material with stack-up, assembly process, and bend testing are presented in the following sections.   Also, the test methods for PCB laminates are presented.

3.1 Printed Circuit Board Assembly (PCBA)

3.1.1 PCB Stack-up & Technical Data

Six commercially available PCB laminate materials typically used in telecommunication products were all constructed to the same stack-up specifications.
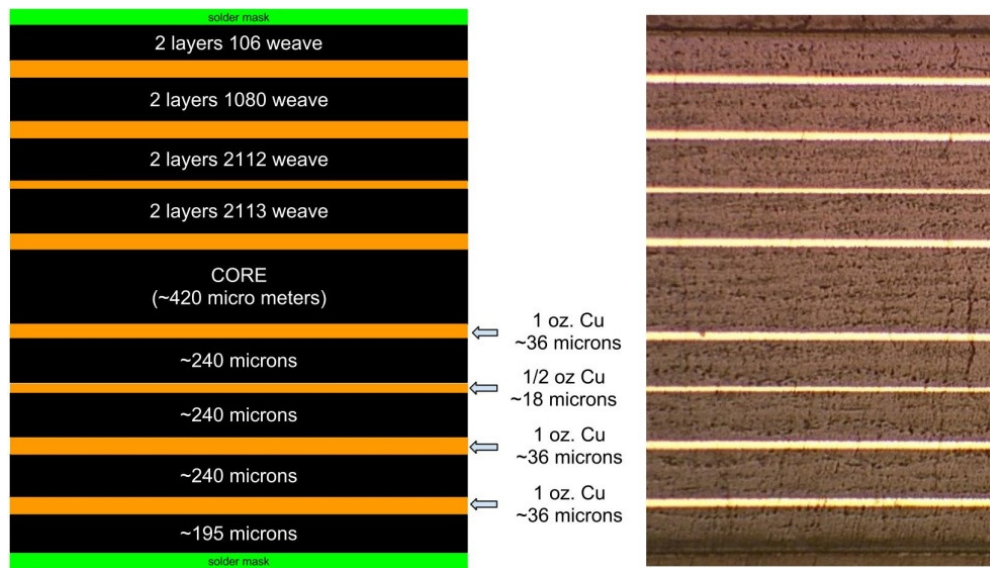
Figure 15: Left: Test Vehicle Stack-up. Right: Example PCB @ 25x magnification under bright field

Figure 15 shows a stack-up schematic of the PCB with weave types along with an actual cross-section image of one PCB.   The PCB stack-up is symmetrical about the core. Two copper weightings present in the PCB are ½ oz. and 1 oz. and nominal thicknesses of copper are 17.1 µm and 34.3 µm, respectively [48].

The available material properties of the PCB are shown in Table 1.   Ideally more material properties would be available, but for proprietary reasons the suppliers keep most information such as precise resin composition, E-glass surface treatments, among others, confidential.

Table 1: PCB Laminate Material Properties

	D	M	G	A	J	B
Resin	PPO* Epoxy Blend	PPE***	Unknown	Phenolic	Phenolic	Phenolic
Halogen Free	No	No	Yes	No	No	No
filler	Inorganic	Inorganic	Inorganic	Inorganic	Inorganic	Inorganic
CTE (x,y)			12~15 ppm/°C			11~15 ppm/°C
CTE (z, % T1°C - T2°C)			< 2.6% (50°C - 260°C)	< 2.8% (50°C - 260°C)		3.4% (25°C - 260°C)
CTE (z)	35 ppm / °C					
CTE (z, pre Tg)			50		50	
CTE (z, Post Tg)			250		266	
CAF (hrs)	> 2000			1000		
Tg (°C) **				< 170	< 170	
Tg (°C, DMA)	215	210				160
Tg (°C, DSC)	176	185	170			150
Tg (°C, TMA)						140
Td > 260 (min)		> 120			60	> 60
Td > 288 (min)	30	> 120			25	> 10
Td > 300 (min)					10	
Td (TGA, °C)	362	410	380			340
Flexural Strength (lengthwise / warp)			420-450 Mpa			> 517 MPa
Flexural Strength (crosswise / fill)			360-390 Mpa			> 448 MPa
Flexural Strength (one value only)						420 Mpa
Moisture Absorption (%)	0.14	0.14	0.07		0.28	0.13
Peel Strength (N / mm)	1.19	0.78	0.7		1.4	1.4

*: epoxy-polyphenylene oxide (PPO)
**: method of measure unknown
***:polyphenelene-ether (PPE)

The test laminates resin systems are phenolic based, PPO epoxy blend, PPE, and halogen-free.

3.1.2 PCBA Assembly Parameters

The stencil used for screening solder paste on the PCBs was stainless steel and 0.127 mm (0.005") thick. Test PCBs had a high temperature organic solder protectant (OSP) finish and the stencil opening was 1:1 with the 0.53 mm (0.021") signal pad.
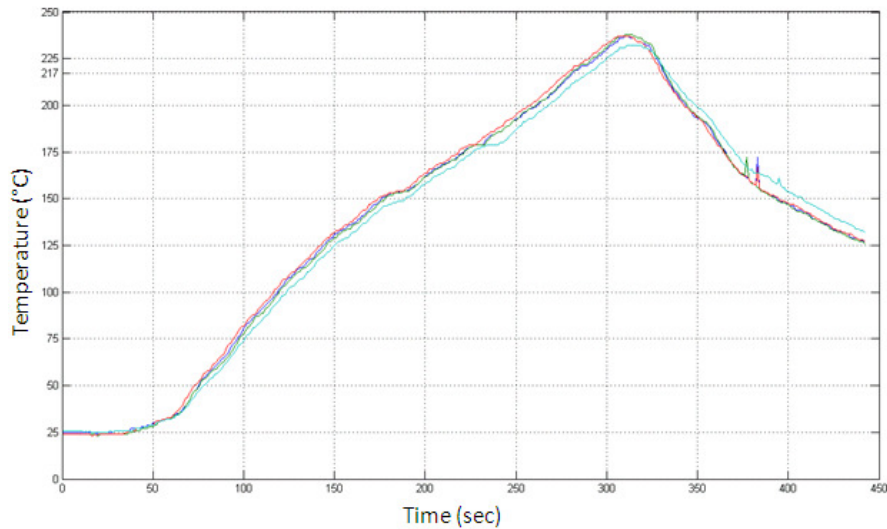
Figure 16: Reflow of PCBA
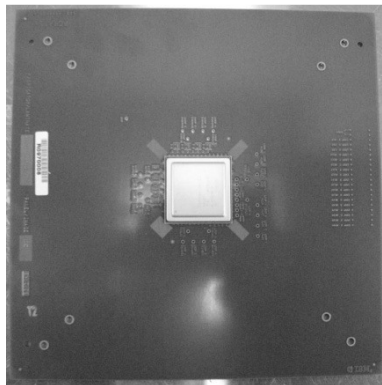
Figure 17: PCBA test vehicle

To simulate a two-sided process, the PCBs were subjected to a bottom side reflow with no component attach. After bottom side reflow, the PCBs were screened by a DEK 265 screen printer with a no-clean Type III solder paste with SAC 387 (Sn, 3.8% Au, 0.7% Cu) alloy. The test vehicles were subjected to the reflow profile in Figure 16 and a sample PCBA is shown in Figure 17. After reflow, PCBAs were kept at 40°C and less

than 5% relative humidity until they were bend tested in order to minimize the effects of moisture absorption for all testing.

3.2 Bend Testing

3.2.1 Spherical Bend Test

IPC/JEDEC 9707, Spherical Bend Test Method For Characterization of Board Level Interconnects [23] was developed in response to the shortcomings of four-point-bend and solder joint level tests, as discussed in Chapter 1. A schematic of the spherical bend test with a PCBA is shown in Figure 18.
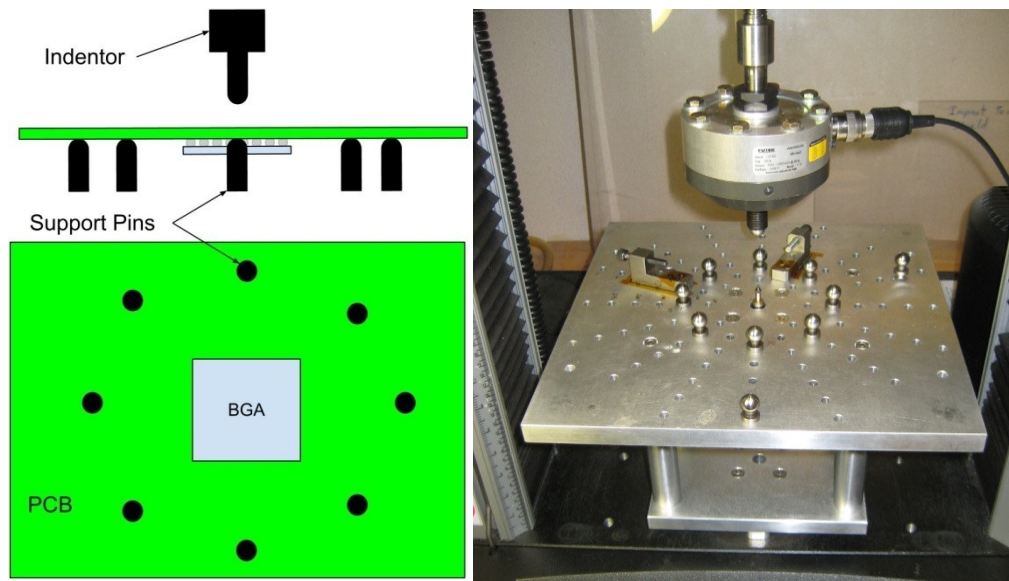
Figure 18: Left: Spherical Bend Test Fixture Schematic, Right: Bend Test Fixture.

During a bend test, the eight support pins are stationary and support the PCBA as the opposing indentor is driven into and flexes the PCBA into a hemispherical shape. The speed and the amount of board deflection are varied to match the conditions the test is intended to simulate. All testing was performed at 3.81 mm / second (9 in. / min) which induces a board level strain rate of approximately 3000 µε / second. Load was

applied to test PCBAs by an Instron 5567 Materials Tester. Linear variable displacement transducer (LVDT) from Transtek (part number 0351-0006) was used to independently measure PCBA displacement for PCB laminates D, M and G. A Futek LCF450 pancake load cell (part number FSH00953) was used to provide input load for PCB laminates D, M and G. PCB laminates A, B and J did not have independent measurement of load and displacement. An upgrade to the test fixture at the midpoint of the testing is the reason for additional data on PCB laminates D, M, and G.

3.2.2 Test Methodology

The test vehicles were subjected to monotonic spherical bend testing in accordance with IPC/JEDEC-9707, Spherical Bend Test Method for Characterization of Board Level Interconnect [23] and PCB level strain was measured in accordance with IPC/JEDEC-9704, Printed Wiring Board Strain Gage Test Guideline [49].
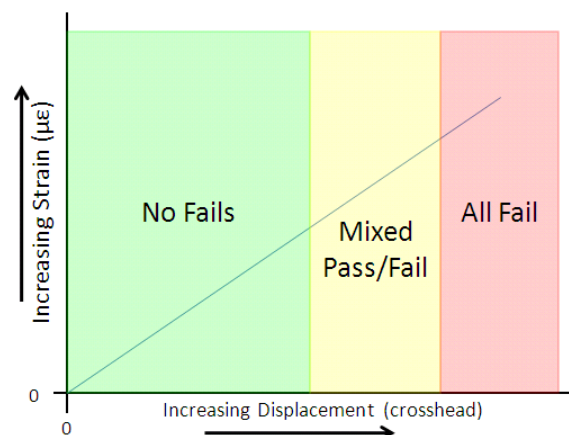
Figure 19: Spherical Bend Test Methodology

Each corner of the BGA is considered to be a test due to the symmetric nature of the test set-up. Since the PCB laminate failures precede electrical opens, the test vehicles were subjected to progressively larger deflections to define three zones: all pass, mixed pass/fail, and all fail. Figure 19 shows a graphical explanation of the bend test

26

methodology. The peak diagonal strain was used as the passing or failing strain for Weibull analysis.

3.2.3 Strain Measurement and Calculations

Ideally, measurement of strain response of a solder joint up to failure would provide good criteria for determining the strain envelope for a PCBA, but BGA solder joints are small and not easily accessible which makes direct measurement of strain economically impractical in industry settings. In the absence of solder joint level strains, PCB level strains adjacent to a solder joint are measured as an indicator in accordance with IPC/JEDEC 9704 [49].

For all strain measurements, linear strain gage CEA-06-125UN-350 and triaxial strain gage C2A-06-031WW-350, both from Vishay Precision Group, were used. Strain was measured with National Instruments NI-9237 strain blocks and bridge excitation voltage of 5.0 volts was used to maximize signal to noise ratio. The frequency of strain measurements was 5000 Hz and custom software written in Labview was used to control the hardware.

For a rectangular rosette, the principal strains were calculated as per equation 3-1.

$$\varepsilon_{p,q} = \frac{1}{\sqrt{2}} \pm \sqrt{(\varepsilon_1 - \varepsilon_2)^2 + (\varepsilon_2 - \varepsilon_3)^2} \quad [50] \tag{3-1}$$

The principal strain angles were calculated as per 3-2.

$$\varphi = \frac{1}{2} tan^{-1} \left(\frac{\varepsilon_1 - 2\varepsilon_2 - \varepsilon_3}{\varepsilon_1 - \varepsilon_3} \right) \quad [50] \tag{3-2}$$

Equation 3-2 returns the minimum or maximum principal strain angle because tan 2φ = tan (2φ + 90). Further data reduction is needed to determine more information about (ε_1–ε_3) to properly determine the maximum principal strain angle [50].

Strain rates were calculated by applying signal windows with a length of 60 data points consecutively over the strain response.   The strain rate of each window was determined by least squares method.

3.2.4 Daisy Chain Continuity

The electrical continuity of a BGA component can be used to monitor the integrity of the conductive paths.   Typically this is done through a Daisy Chain and for a BGA component, the outermost leads form the conductive path.   The conductive path alternates between the BGA and the PCB so failure at either will cause an open circuit. Figure 20 shows a schematic of a daisy chain in a BGA component with a power supply (V) and voltmeter (VM).
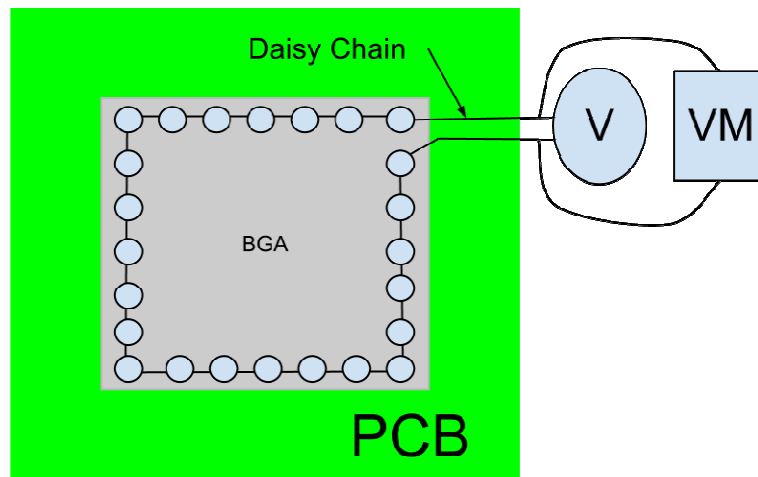
Figure 20: Daisy Chain Circuit

The power supply provides a constant current power source and the measured voltage across the conductive path is divided by the current to calculate the resistance (Resistance = Volt / Current).

For all experiments, a constant current of 0.1 amps with 5.0 V peak was applied to the daisy chain circuit by a HP 6632A power supply and daisy chain resistance was measured with NI-9239 A/D converter. Custom software written in Labview was used to control the measurements and daisy chain resistance was calculated by dividing the applied voltage by 0.1 amps to get resistance of the circuit. A resistance increase of 20% was considered an electrical failure.

3.2.5 Dye and Pry for detection of Pad-Crater failure

The process of finding pad-crater cracks involves submerging a PCBA in Dykem Steel Red Layout Fluid and cycling in a vacuum chamber to 27 mmHg (3.6 kPa) vacuum. The applied vacuum draws air out, and liquid into any existing crack. After the vacuum cycle, the PCBA is placed in an oven at 60°C for 30 minutes to dry the dye to the PCBA. The BGA component is then removed by prying it away from the PCB.   The drawbacks of this process are that the pry event is violent and causes significant damage to the PCB, the crack must have had access to the liquid during the vacuum process, and the crack must have existed on a 2D plane that is visible after the pry event.   For all of its drawbacks, dye and pry is a widely used process for detecting pad-crater defects in the electronics industry.

3.3 PCB Laminate Properties & Characteristics

3.3.1 Tensile Properties of PCB Laminate

The tensile properties were measured as per ASTM standard D638M—10, Standard Test Method for Tensile Properties of Plastics [51], with dumb bell coupons as shown in Figure 21 and corresponding dimensions shown in Table 2.

Table 2: ASTM 638-10 Coupon Dimensions in mm

W	L	G	R	Wc	Lo	D
13	57	50	75	W (+0/-0.1)	165	115
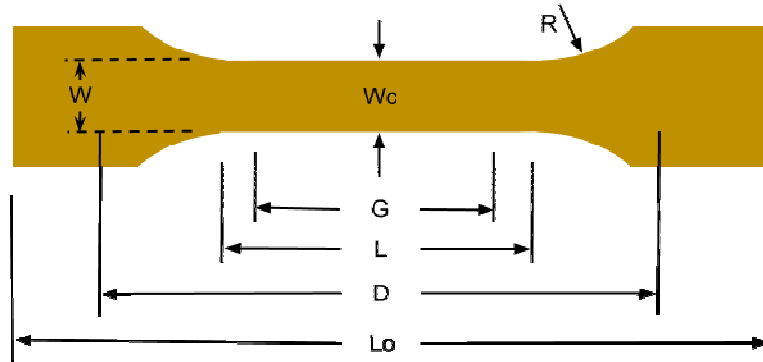
Figure 21: Dumb bell coupon as per ASTM 638-10

The dumb bell coupons were cut from test PCBs so there is resin, E-glass and copper present as shown in Figure 15. Cross-head speed was 5 mm / min and tests were run to 2000 με.

3.3.2 Micro-indentation Hardness

The micro-indentation of PCB boards was made in accordance with E 384-10, Standard Test Method for Micro-indentation Hardness of Materials [52]. A Buehler Micromet ® 5103 was used to apply an indentor force of 10 grams with a test duration of 10 seconds, a protocol used by other investigators [7]. Each PCB laminate was measured a minimum of 32 times.

The samples were prepared from test boards by cutting away portions of the boards adjacent to the BGA signal pads. The samples were then potted and ground with Leco 1 μm diamond grit (part number 810-870) to remove the solder mask and expose the resin. Care was taken to ensure the grit did not contain any water which might have

30

affected the measurements. Measurements were made on PCB laminate immediately adjacent to the BGA site.

3.3.3 PCB Laminate Tow and Buttercoat Measurements

Measurement of tow geometry was performed in accordance with IPC Test Method 2.2.2 [53].
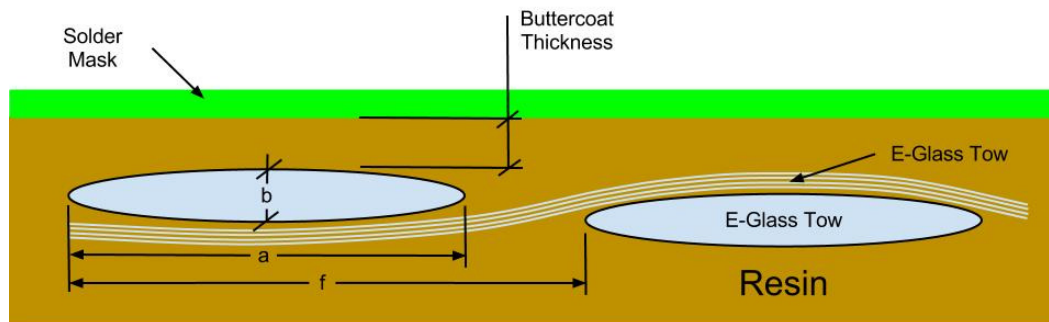
Figure 22: Buttercoat thickness schematic

The thickness of the buttercoat—the resin rich layer between the first layer of E-glass weave and the top of the PCB—was measured as the minimum distance between the tow and the top of the board as shown in Figure 22. The tow dimensions a, b and f were measured as the distance between the outermost E-glass strand, even if it was slightly separated from the tow.

Chapter 4: Results, Analysis and Discussions

4.1 PCB Laminate Properties

4.1.1 Young's Modulus (E) Results

A probability plot of the Young's modulus (E) for all PCB laminates is shown in
Figure 23. E was determined by secant method because the stress-strain curve was not
linear for all tests.
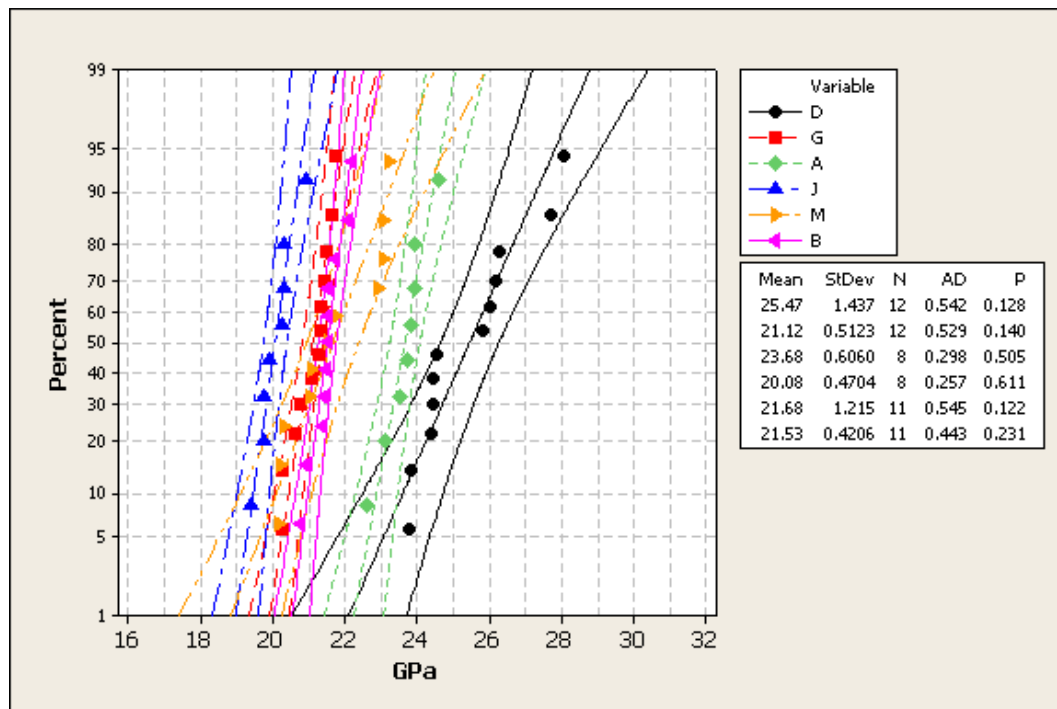
Figure 23: Probability Plot of Young's Modulus

Points at 250 με and 2000 με were used for the secant method because they represent
the failing range for all PCB laminates.   Figure 23 shows the normal probability plots
with 95% confidence intervals (CI) of all E values with mean, standard deviation,
sample size, Anderson Darling, and P values shown.   The minimum sample size of five
was reached for all samples as per ASTM D638-10 [51].

4.1.2 Young's Modulus (E) Analysis

The PCB laminate with the lowest mean E value was J at 20.08 GPa, and it was the third most resistance laminate to pad-crater. PCB Laminate A and D had highest E values of 23.68 GPa and 25.47 GPa respectively, and they represent two of the three least resistant laminates to pad-crater. Two sample t-test shows that PCB laminates A and D are statistically different from the other laminates to a confidence level of 0.05. PCB Laminate B, the most resistant to pad-crater, had an E value of 21.53 GPa, which is almost identical to the second worst performing laminate G at 21.12 GPa.

The measured E values for the test coupons include the plated copper from the PCB. The theoretical E of the PCB laminate only can be calculated as follows [54]:

$$P = P_{Cu} + P_{Lam} = \frac{\delta}{L}(A_{cu}E_{Cu} + A_{Lam}E_{Lam})$$

4-1

Where P is load, A is area, E is Young's modulus, and δ is elongation. By rearranging terms of equation 4-1, the E of the PCB laminate can be calculated:

$$E_{Lam} = \frac{\frac{PL}{\delta} - A_{Cu}E_{Cu}}{A_{Lam}}$$

4-2

The E values for the PCB laminate were calculated with the assumption that the copper in the PCB has a Young's modulus of 100 GPa [46] and the thickness of the PCB laminate equaled the measured thickness minus the nominal copper thickness. The normal probability plots of all theoretical E values are shown in Figure 24 with 95% CIs. The order of PCB laminate E values did not change with the removal of the copper. PCB laminate D showed the largest variation in E values with a standard deviation of

1.221 GPa. In Figure 24, the samples from the same PCB have been circled with like lines for PCB laminate D.
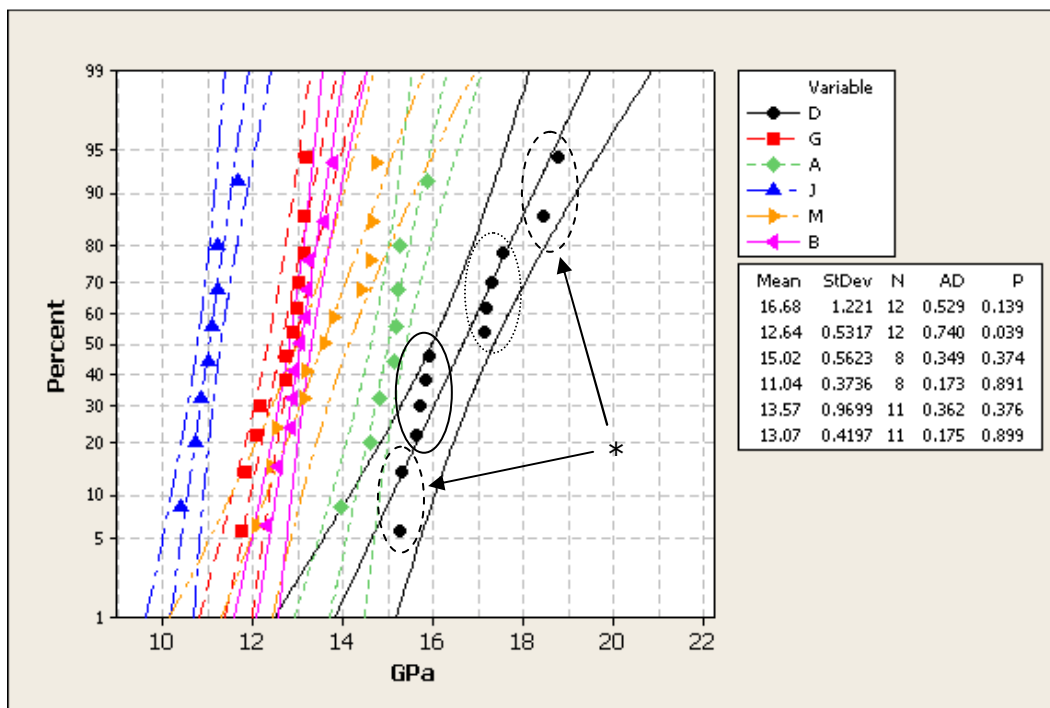
Figure 24: Theoretical Young's Modulus for PCB Laminate Only

Most notable is the * samples from the same PCB with Young's Modulus values that range from 15.2 to 18.8 GPa. For these samples, the thickness ranged from 2.3 mm for the higher E values to 2.7 mm for the lower E values. This variation in sample thickness represents the maximum variation allowable (±10%) for a PCB. To further investigate the variation of PCB laminate D results, load vs. strain curves for all tests and probability plots of peak load were plotted and are shown in Figure 25 and Figure 26. As can be seen from these figures, there is little variation between the samples as shown by the load vs. strain curves and the normal distribution of the peak loads. Consequently, the high E values of PCB laminate D are real and not the results of dimensional variation of the samples.
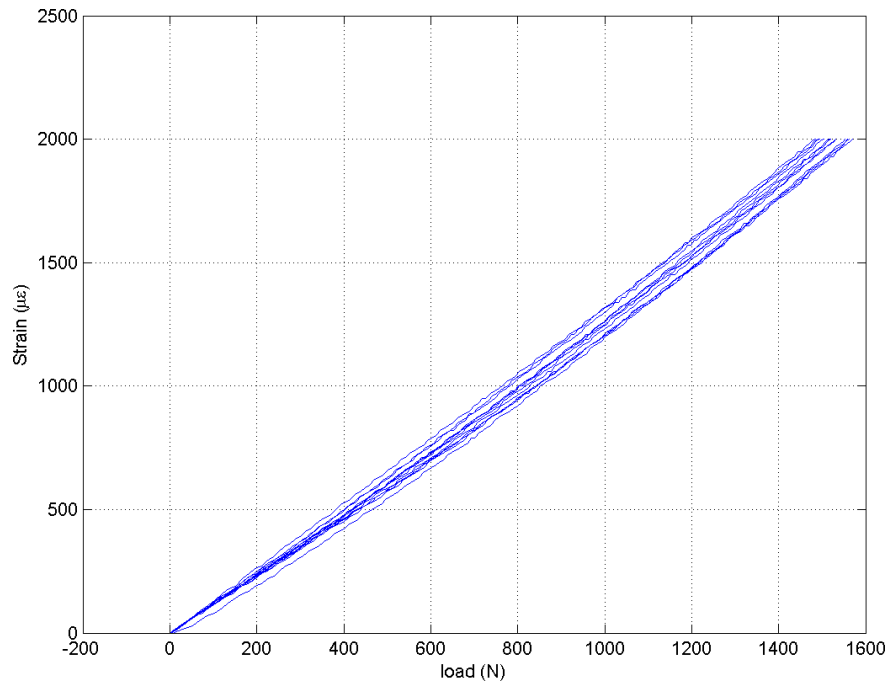
Figure 25: Load vs. Strain of Young's Modulus Tests, PCB Laminate D
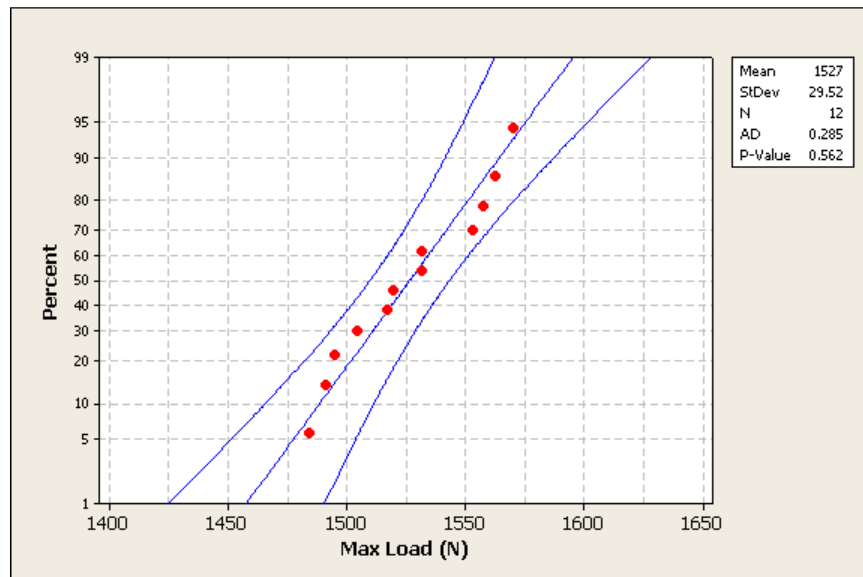
Figure 26: Normal Probability plot of peak load to 2000 με of PCB laminate D

The PCB laminate with the highest E value, laminate D, was also the only PPO resin blend. A relationship between PCBA level strain and Young's modulus can be reasoned by considering two PCB laminates of Young's Modulus values of E_1 and E_2, where $E_1 >> E_2$. For the E_2 laminate, the presence of the BGA provides a significant increase in

35

stiffness which forces the deformation to outside the BGA. The increased stiffness in the BGA area keeps the combined BGA/PCB section relatively flat, which makes radius R_{E2} small.
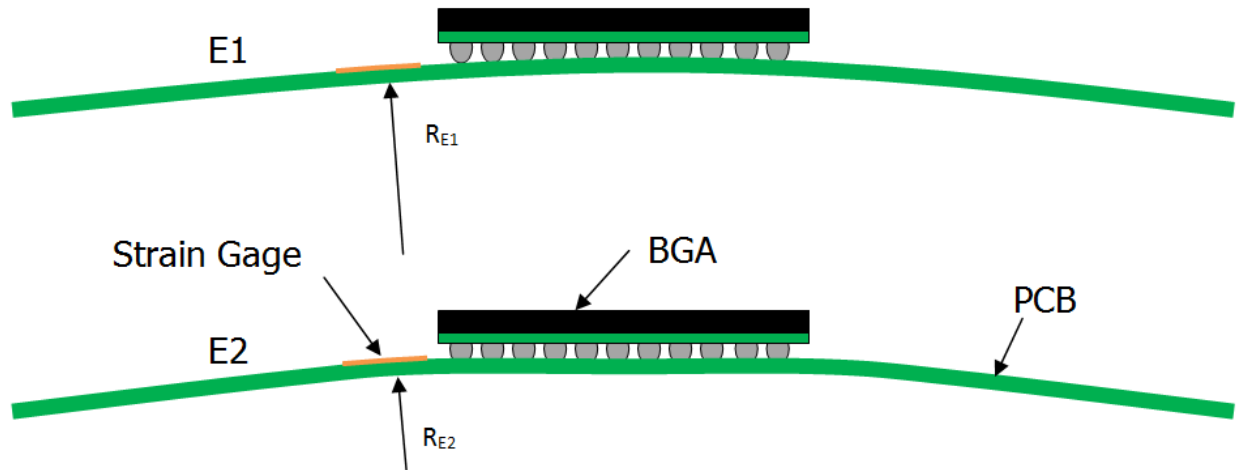
Figure 27: Spherical Bend for E1 and E2 (E1 >> E2)

The relationship between surface strain and the bend radius of a plate or beam is inverse ($\varepsilon \propto 1$ / radius of curvature). Conversely, for E_1 laminate where the BGA does not provide a significant increase in stiffness, the bend radius inside and outside the BGA shadow area would be closer in value, and as a consequence, larger. This relationship between radius of curvature and PCB E values is illustrated in Figure 27.

For the three laminates that had LVDT measurements of board deflection, a comparison of strain slopes can be made. The PCBA level strain as a function of displacement was determined by least squares linear regression for PCB laminates D, G and M. The R^2 for all linear regression was > 97%, showing the model is a good fit. The normal probability plot with 95% CI of slope values ($\mu\varepsilon$ / mm) is shown in Figure 28. As the figure shows, PCB laminate D is statistically different than G and M.
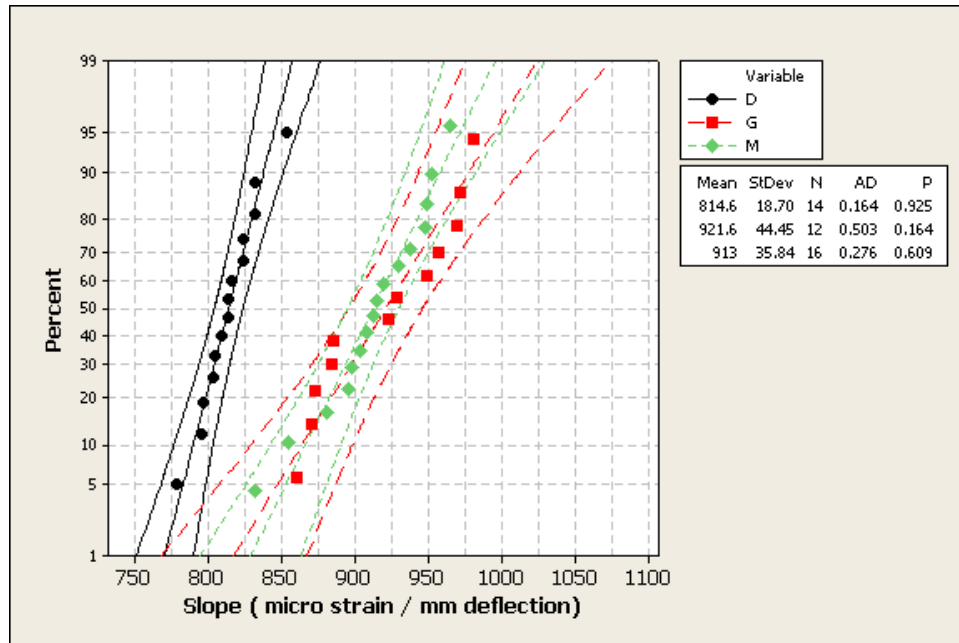
Figure 28: PCB Laminate D, G & M Slope (με / mm deflection)
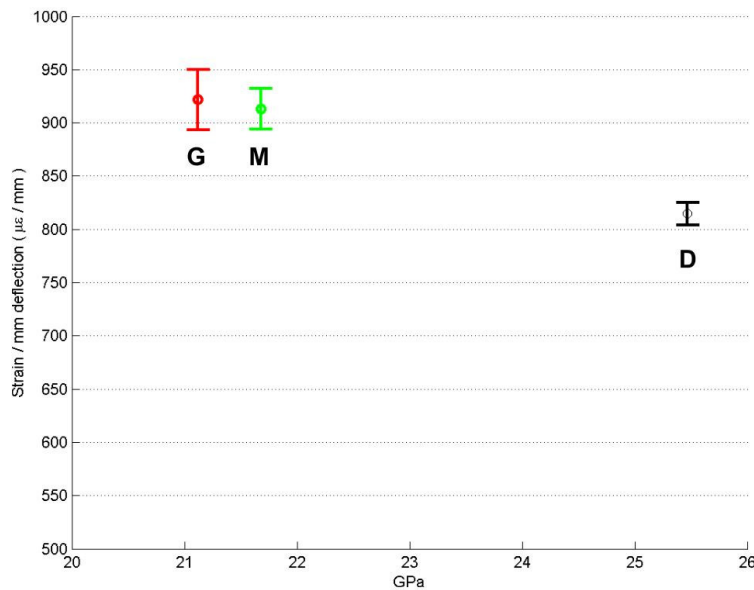
Figure 29: 95% Confidence Interval of PCB Laminate D, G & M mean με / mm slope vs. mean E

A plot of the 95% confidence intervals of the average με / mm slope vs. average E value for PCB laminate D, G and M is shown in Figure 29. As can be seen from this plot, there is clearly an inverse correlation between the με / mm slope vs. PCB laminate average E. This inverse correlation confirms the reduced radius of curvature at the strain gage location for PCB laminates with lower E values.

4.2 Spherical Bend Test

For the spherical bend testing, pure laminate G10, bare PCB, and PCBAs were tested. The G10 pure laminate is a plain weave laminate without any copper or vias present. Two bare PCBs from the six test PCB laminates were reflowed without component attached and bend tested. PCBAs from each test laminate were tested to determine fail free, mixed fail, and all fail zones. Finally, the Weibull analysis of all six PCBA pad-crater results was performed. All testing was performed at 3.81 mm / sec cross head speed. For pure laminate and bare PCB, cross-head travel was 1.0 mm.

4.2.1 Pure Laminate

4.2.1.1   Test Set-up

The strain gage layout for the G10 board is shown in Figure 30.
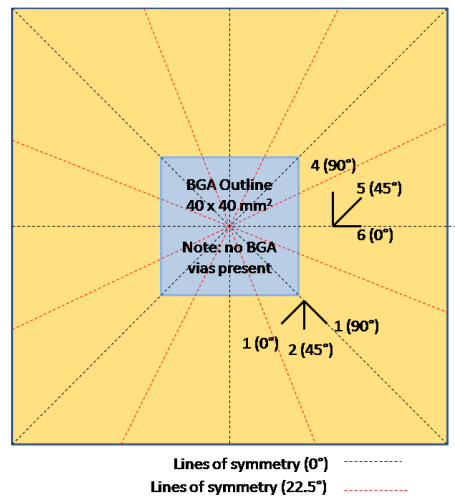
Figure 30: Laminate Strain Gage Layout with strain channels and gage numbers

The strain gages were placed 32 mm from the center of the board. Lines of symmetry for fixture orientation have been added to Figure 30 to show the strain gage location relative to pin supports. In order to investigate whether or not the eight support pins

can be modeled as a simple continuous support, tests were conducted at 0° and 22.5^o sample orientation as shown in Figure 31.
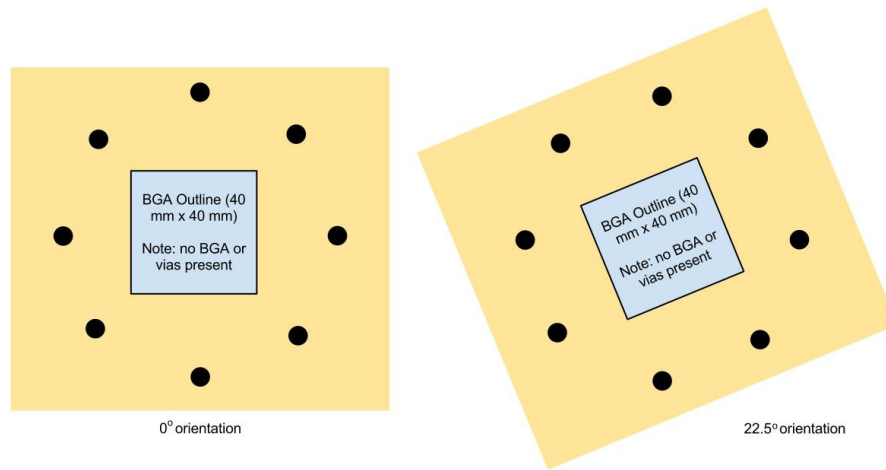
Figure 31: 0º and 22.5º sample orientation

4.2.1.2   Pure laminate Results

Figure 32 shows the max principal strain (PS) angle of gage 1 (ε123) and gage 2 (ε456) vs. displacement, and as can be seen from the plot, the PS angle asymptotically approaches the circumferential strain direction θ(0° for gage 1, and 90° for gage 2).
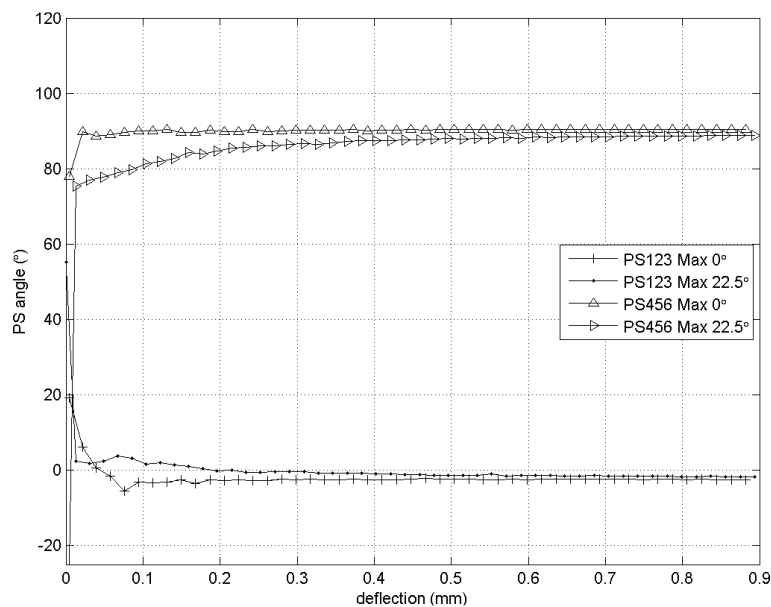
Figure 32: Max Principal Strain angle of ε123 and ε456 for pure laminate

For the 22.5° sample orientation, both gages initially show more variation from the θ direction.
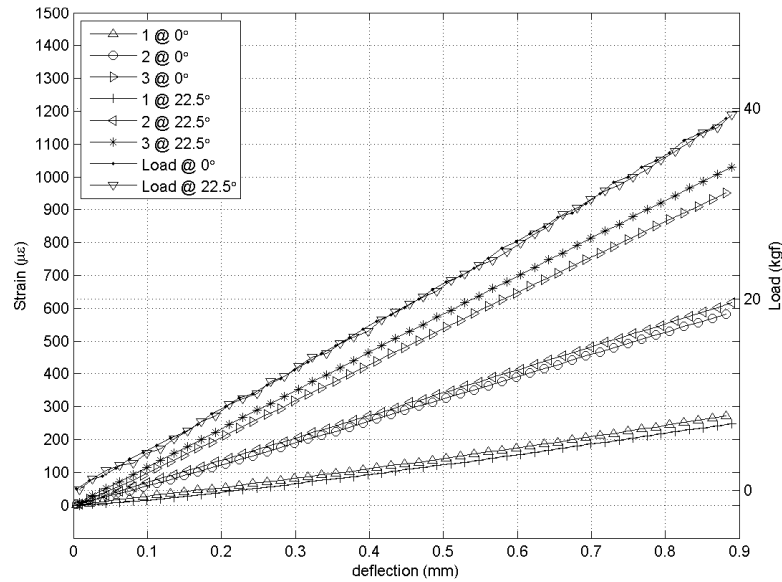
Figure 33: Pure Laminate Spherical Bend Test Comparison of strain (gage 1) and load vs. displacement at 0°and 22.5°
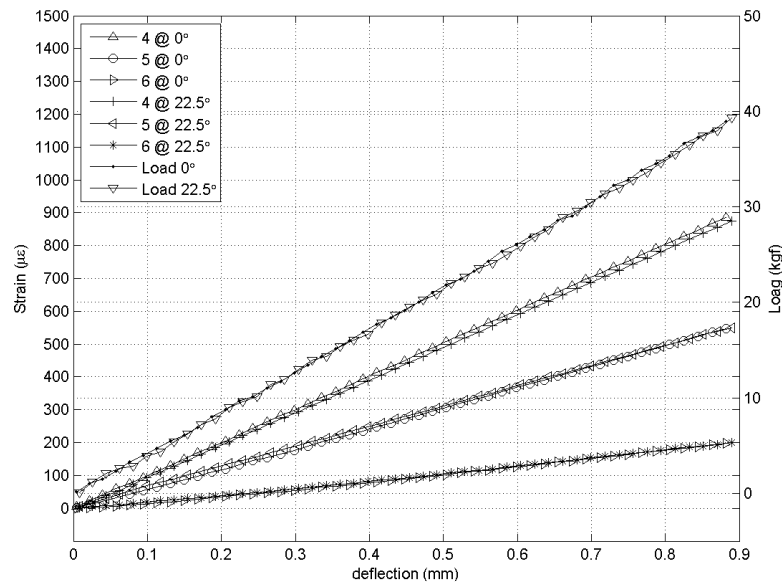
Figure 34: Pure Laminate Spherical Bend Test Comparison of strain (gage 2) and load vs. displacement at 0°and 22.5°

Figure 33 and Figure 34 show gage 1 and 2 strain responses vs. displacement for 0° and 22.5° sample orientation. Comparison of the responses shows that in general, the magnitude of gage 2 ($\varepsilon456$) is less than gage 1 ($\varepsilon123$) for both sample orientations.

The variation in strain response is almost negligible for gage 2 between sample orientations, but for gage 1, it is considerable, especially at ε3. This could be the result of slight differences in the distance in the gages from the center of the applied load, and errors in gage placement. The more likely reason is reduction in stiffness Q for orthotropic material from on-axis to off-axis orientation. Note that gage 2's axes are aligned to the plain weave, and gage 1's bisects the plain weave.

4.2.1.3 Pure Laminate Analysis

The maximum and minimum principal strains are shown in Figure 35 for 0° and 22.5° sample orientation.
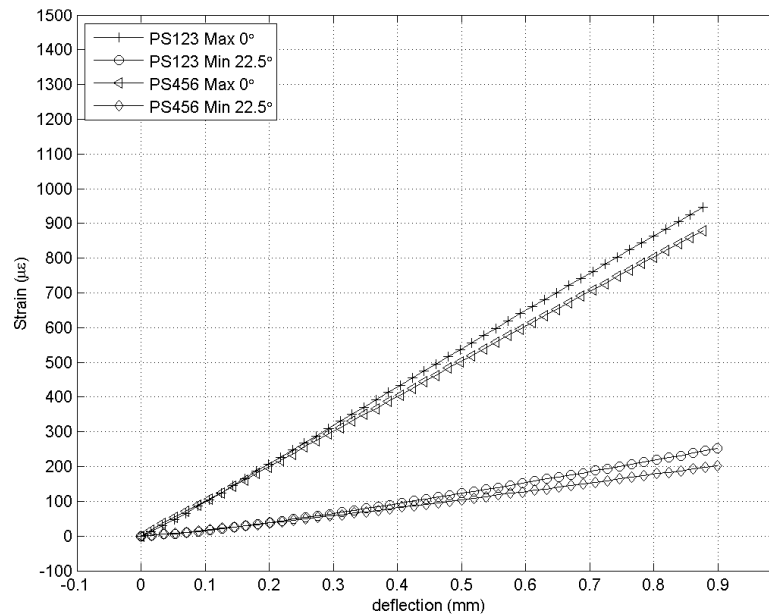
Figure 35: PS max and PS min vs. displacement for Pure Laminate

In both orientations, gage 1 (ε123) response is larger than gage 2 (ε456), despite the fact that both gages are the same distance from the center of the G10 sample. Transformation of in-plane stiffness for orthotropic materials can be calculated by equation 4-3 [55].

$$Q_{11} = m^4 Q_{xx} + n^4 Q_{yy} + 2m^2 n^2 Q_{xy} + 4m^2 n^2 Q_{ss} \qquad \text{4-3}$$

Where m = cos(θ) and n = sin(θ).

A complete set of material properties for G10 was unavailable so for comparison purposes, FR4 published properties were used to calculate the transformation of stiffness for orthotropic material and the results are shown in Figure 36 [25]. The on-axis stiffness varies from 20.8 GPa at 0° to 19.5 GPa at 45°. This reduction in stiffness can explain the increased response of gage 1 since ε1 and ε3 are oriented at 45° to the direction of weave.
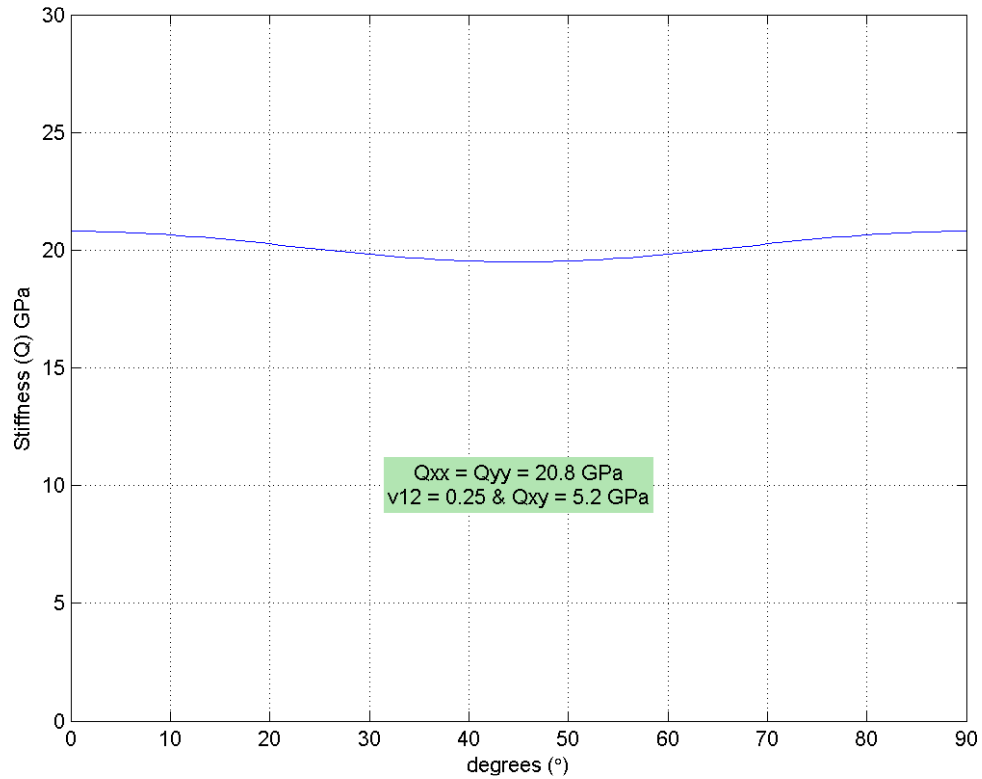
Figure 36: Transformation of stiffness for plain weave laminates

Plain weave laminate can be treated as an isotropic material due to the balanced nature of its properties [45]. Equations 4-4, 4-5, and 4-6 are the theoretical displacement, radial, and circumferential stress for a simply supported circular plate

with a concentrated load at the center [56]. A poisson ratio equal to 0.34 was used for these calculations [47]. The distance from the neutral axis is z, the distance from center of the plate is r, and a is the radius of the support. These equations are based on the assumption that there is zero shear and are applicable for plates with small transverse displacements.

$$w = \frac{P}{16\pi D}\left[2r^2 \ln\left(\frac{r}{a}\right) + \left(\frac{3+v}{1+v}\right)(a^2 - r^2)\right]$$ 4-4

$$\sigma_r = \frac{3Pz}{\Pi t^3}\left((1+v)\ln\left(\frac{a}{r}\right)\right)$$ 4-5

$$\sigma_\theta = \frac{3Pz}{\Pi t^3}\left((1+v)\ln\left(\frac{a}{r}\right) + 1 - v\right)$$ 4-6

Inspection of equations 4-5 and 4-6 reveals the only difference between the two equations is the (1-v) term in 4-6 which ensures that σ_θ is always greater in magnitude than σ_r. Since σ_θ and σ_r are mutually orthogonal, maximum PS angle will always be in the θ direction. This result is confirmed by the PS angle results previously shown in Figure 32. A comparison of theoretical and measured values using the above equations for gages 1 and 2 is shown in Table 3. Theoretical values in the Table 3 were calculated based on the input force by the Instron 5567. As Table 3 shows, there is good agreement between theoretical and measured strain values for $\mu\varepsilon_\theta$ at gage 2. The percentage difference for ε_r at gage 2 is consistent at -14% and -12% for 0° and 22.5° orientation. For gage 1, there is a significant error for ε_θ, especially at 22.5° orientation. The increased error is likely due to increase radius of curvature when the gage is located between two support pins. This increased radius of curvature can also help to explain the reduction in ε_r error from 19% to 9% between 0° and 22.5°

orientation at gage 2.   The positive difference in $\mu\varepsilon_r$ at gage 1 and negative difference

at gage 2 can also be explained by variation in G10 stiffness shown in Figure 36.

Table 3: Comparison of measured and theoretical strain values of pure laminate plate

		Gage 1		Gage 2	
	w (mm)	$\mu\varepsilon_r$	$\mu\varepsilon_\theta$	$\mu\varepsilon_r$	$\mu\varepsilon_\theta$
Theoretical 0°	0.88	234	859	234	859
Measured 0°	0.90	278	968	202	900
% difference 0°		19	13	-14	5
Theoretical 22.5°	0.88	235	863	235	863
Measured 22.5°	0.91	256	1049	206	891
% difference 22.5°		9	22	-12	3

4.2.2 Bare PCB Spherical Bend Test at Sample Orientation 0° and 22.5°

4.2.2.1   Test Set-up

Bare board response of the PCB was investigated with two rosette strain gages as

shown in Figure 37 for PCB laminate A and B.
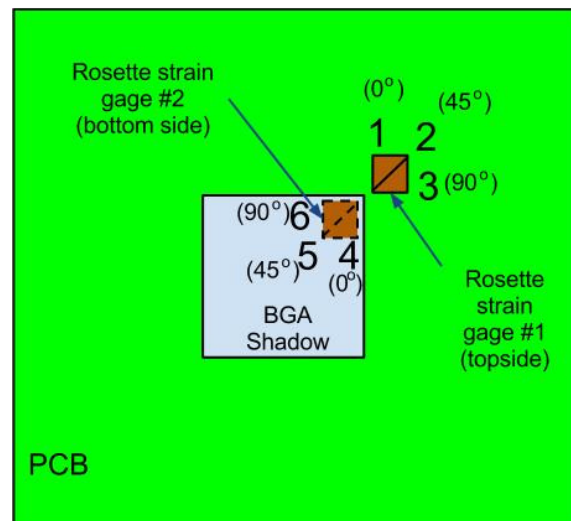
Figure 37: Bare PCB Strain Gage Layout

Placement of gage 1 was identical to the placement of all PCBA testing and the gage 2

was on the bottom side of the PCB at the edge of the BGA shadow. Testing of gage 1

at sample orientation 0° and 22.5° and gage 1 and 2 at 0° was performed. Comparison

of the response of gage 1 at sample orientation 0° and 22.5° is presented. Also, comparison of gage 1 and gage 2 responses to theoretical values is presented at sample orientation 0°.

4.2.2.2   Results and analysis for sample orientation 0^0 and 22.5^0 for gage 1

The strain and max PS angle responses for PCB laminate A and B are shown Figure 38 and Figure 39 respectively for gage 1.
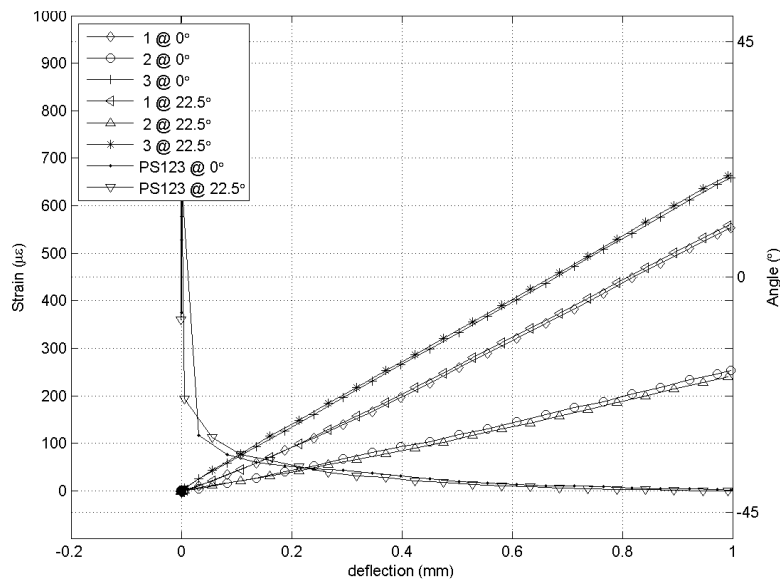
Figure 38: Comparison of rosette strain gage 1 for 0° and 22.5° fixture orientation, PCB Laminate A

As can be seen for both fixture orientations, the PS max angle for gage 1 is in the θ direction (-45^0).   PCB laminate A shows a consistent difference in strain response at gages 1 and 3 for both orientations and PCB laminate B does not.   This could be due to differences in material properties in the warp and fill direction for PCB laminate A. PCB Laminate B (Figure 39) shows bilinear behaviour with the diagonal strain initially being negative, and the change in response occurs at roughly 0.12 mm deflection. Laminate B is the best performing laminate and this initially negative strain could apply

less stress to the corner BGA solder joints.   For both laminates, there is negligible difference in the magnitude of strain response for either fixture orientation.
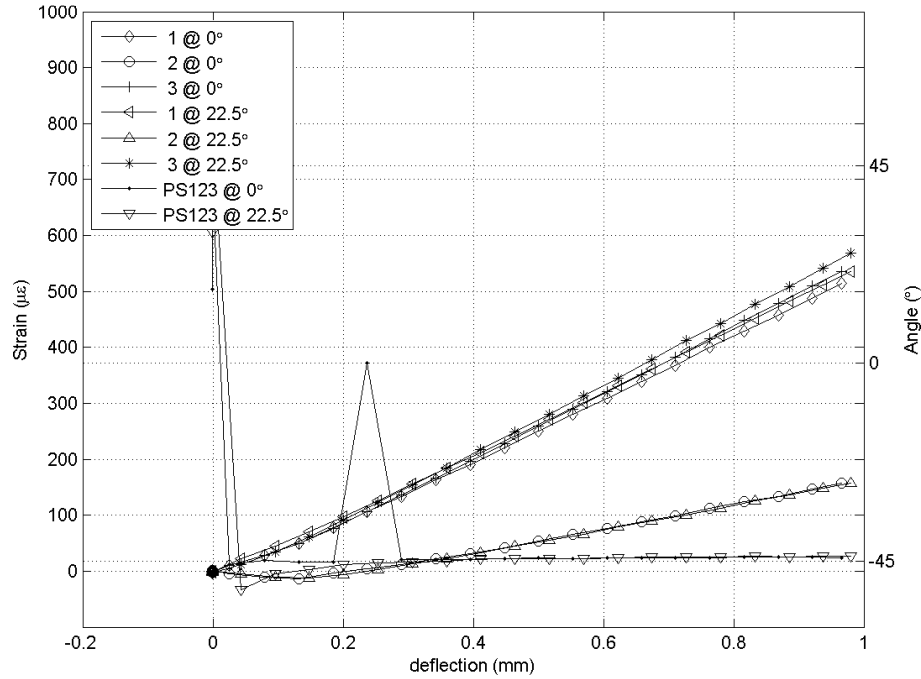
Figure 39: Comparison of rosette strain gage 1 for 0° and 22.5°, PCB Laminate B

4.2.2.3   Results and Analysis of Bare PCB Bend Test for gage 1 & 2 at 0° sample orientation

Using equations 4-4, 4-5, and 4-6, the theoretical strain at gage locations 1 and 2 were calculated using the mean Young's modulus test values for PCB laminate A and B. All calculations were made assuming the same material properties inside and outside the BGA shadow area. Load input value P for equation 4-4 was taken from LVDT load measurements to determine theoretical displacements.   The measured ε_θ were calculated by transformation of rectangular rosette strains ε_1, ε_2 and ε_3 by equation 4-7 [57].

$$\varepsilon_{x'} = \varepsilon_1 cos^2\theta + \varepsilon_3 sin^2\theta + (2\varepsilon_2 - \varepsilon_1 - \varepsilon_3)\, sin\theta cos\theta \qquad \textbf{4-7}$$

Plots of theoretical and measured strain responses vs. displacement for PCB laminate A

and B are shown in Figure 40 and Figure 41, and a summary of peak responses is

shown Table 4.

Table 4: Summary of theoretical and measured strain responses at gage 1 & 2, bare PCB strain, laminate A & B

	A		B	
	gage 1	gage 2	gage 1	gage 2
w (measured)	0.997		1.00	
w (theoretical)	0.98		0.877	
% difference	-1.7		-14.0	
$\mu\varepsilon_\theta$ theoretical	908	-1035	813	-926
$\mu\varepsilon_\theta$ measured	962	-1229	911	-1166
% difference	5.6	15.8	10.8	20.6
$\mu\varepsilon_r$ theoretical	362	-49	324	-438
$\mu\varepsilon_r$ measured	254	-224	163	-146
% difference	-42.5	-118	-98.8	-200

Comparison of theoretical and measured deflections for input force shows good

agreement with laminate A, but B shows a -14% difference. For gage 1 on both

laminates, measured ε_θ is larger than the theoretical and measured ε_r is lower than the

theoretical. This suggests the σ_r response of the weakened BGA shadow area is not

balancing the σ_θ response as happened with the G10 material. The theoretical solution

is not sufficient to describe the response of the bare PCB with a weakened BGA shadow

area.

For gage 2, both PCB laminate A and B ε_r responses become non-linear, with

laminate B's ε_r being initially bilinear. This results in a percentage difference of -118%

and -200% between the theoretical and measured values for laminate A and B

respectively.
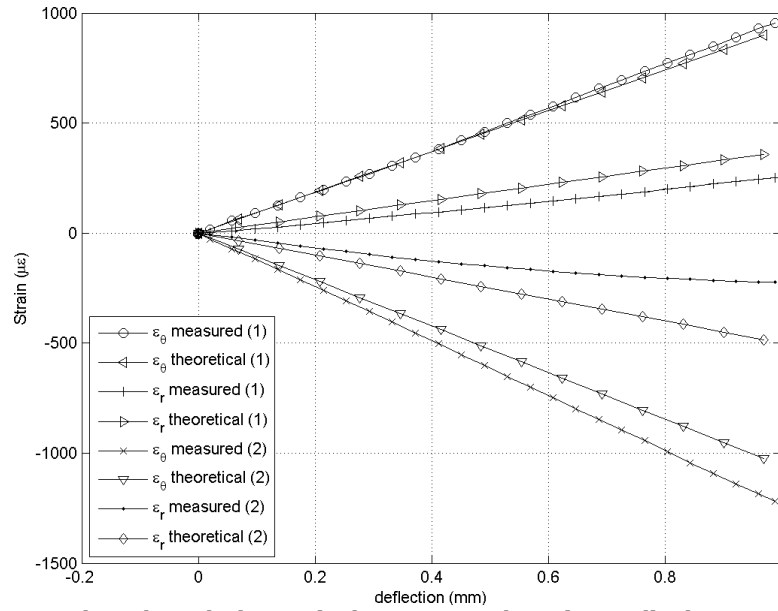
Figure 40: Laminate A bare board, theoretical & measured strain vs. displacement, gage (1) & (2)
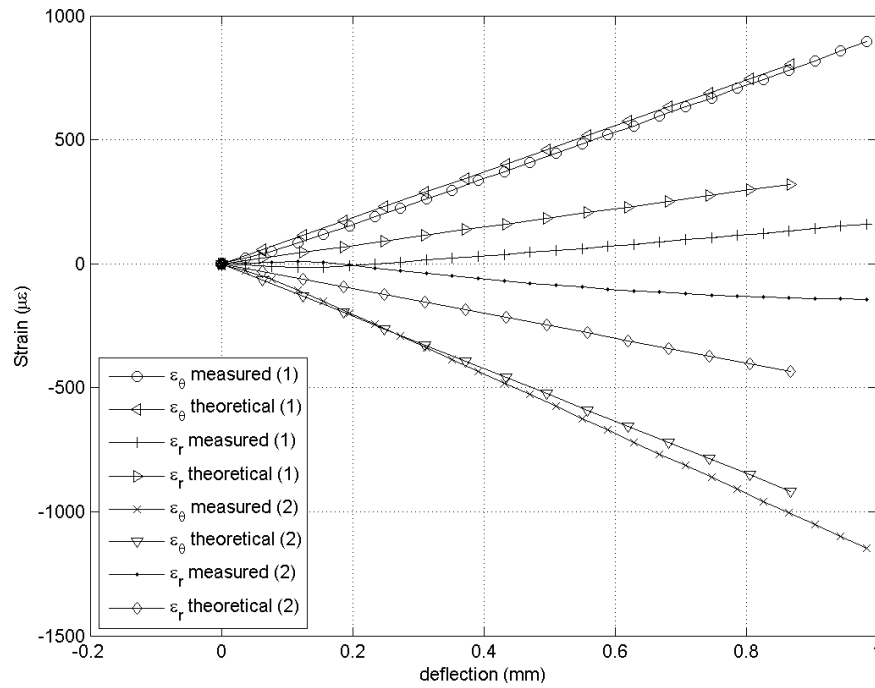
Figure 41: Laminate B bare board, theoretical & measured strain vs. load, gage (1) & (2)

The ε_θ responses are linear at gage 2 for both A and B, but the theoretical values are smaller than the measured values. There are likely two phenomena contributing to the non-linear responses: material non-linearity of the laminate and geometric non-linearity of square BGA shadow area in spherical bend.

4.2.3 PCBA Spherical Bend Test

4.2.3.1   Test Set-up

The strain gage layout of the test board is shown in Figure 42. There are three linear strain gages and one tri-axial strain gage on each test vehicle.
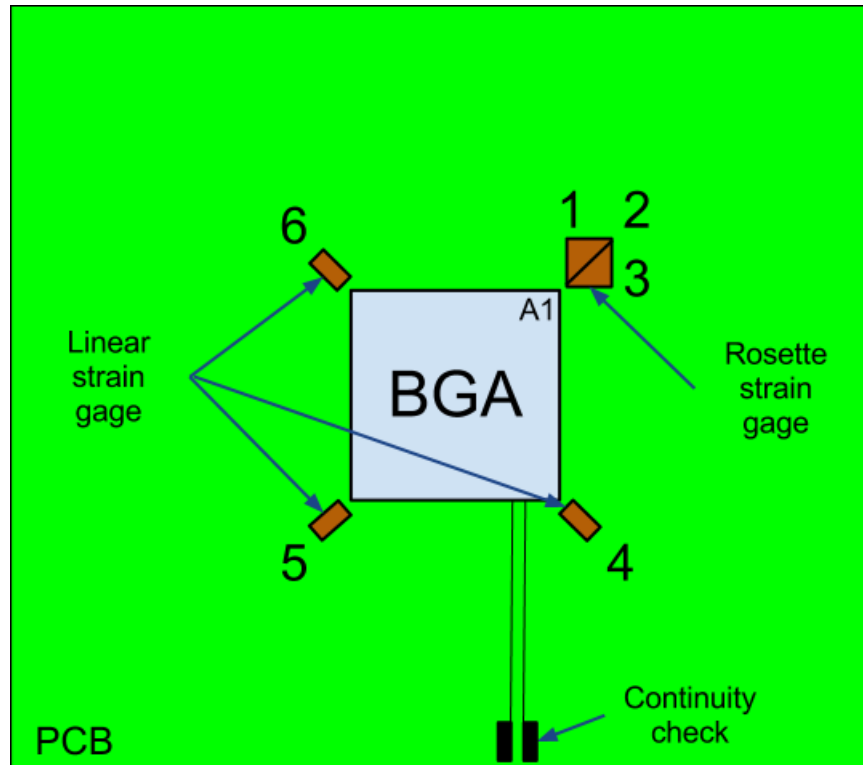
Figure 42: Strain gage layout

Only one rosette is required to determine PS angle at corner A1 due to PCBA symmetry. Sample strain and max PS angle responses are shown in Figure 43 and strain rates in Figure 44 for one test on PCB laminate D. These responses are typical of all tests that were performed on the six test laminates.
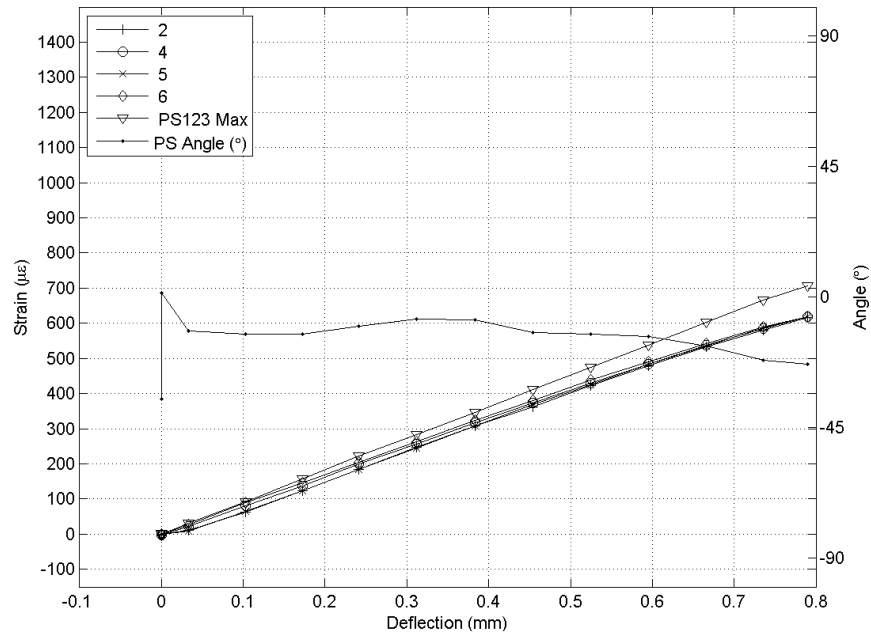
Figure 43: Sample 382, All Strains and Max PS angle vs. Displacement
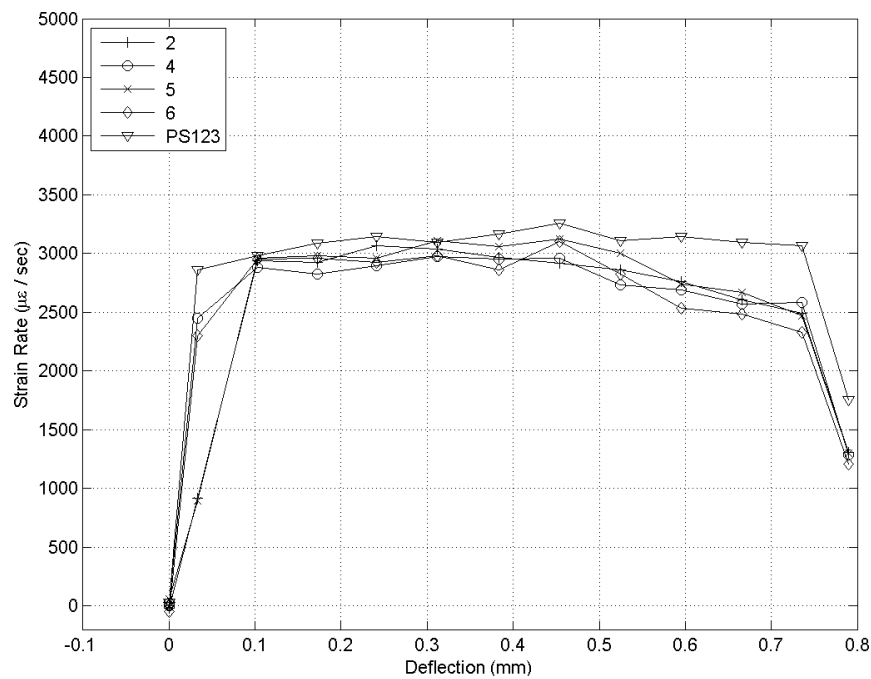
Figure 44: Strain rate responses for one bend test of Laminate D

4.2.4 Daisy Chain Continuity Results and Analysis

There were no opens on any test performed on any PCBA confirming the results of previous investigators [7, 9, 10, 14].

4.2.5 PCBA Pad Crater Weibull Analysis

The suspended or failing strains for all six laminates are shown in Table 5.

Table 5: Surviving and Failing micro strain for all PCB laminates

Laminate A	Laminate B	Laminate D	Laminate M	Laminate G	Laminate J
-659	-967	-415	-999	796	796
-702	-1025	-423	-1046	-895	-895
-716	-1031	-434	-1057	-933	-933
-730	-1071	-462	1070	-948	-948
-782	-1109	-475	-1070	-949	-949
793	-1167	-486	-1085	-996	-996
795	-1218	-502	1087	999	999
-830	-1238	508	-1091	-1005	-1005
830	-1368	-514	-1110	1036	1036
-839	-1402	-519	1116	964	964
-846	-1436	-520	-1117	-1053	-1053
-858	1446	-552	1117	-1054	-1054
879	1454	560	1117	1060	1060
-886	1469	586	1124	-1069	-1069
902	-1488	-610	1130	1072	1072
907	1493	625	1132	1079	1079
-924	1496	-627	1138	1082	1082
933	-1497	629	1139	1092	1092
942	1515	630	-1154	1097	1097
-942	-1516	-659	1155	1112	1112
960	-1534	-702	1166		-1114
977	-1559	-704	1174		-1135
1010	1567	704	1175		1139
1029	1582	736	1180		-1139
1046	-1590	743	1193		1145
1076	1596	807	-1196		1156
1102	1617		-1217		1172
1116	1643		1221		1178
1134	1650				1218
1184	1664				-1267
-1189	1666				1271
1129	1686				1276
	-1691				
	1760				
	-1763				

The negative values represent suspensions and the positive values represent failures. BGA corners that did not fail were considered as suspensions and treated as such for calculation of β and η values of the two parameter Weibull distribution. Waloddi Weibull's original derivation of the Weibull distribution was premised on the idea that if a system is considered to be a series of chain links and any link in the chain fails, then

the system has failed. In such a system, if P represents the probability of one link failing, we can let P_n represent the probability of failure of any link in the chain. Conversely, $(1-P_n)$ or $(1-P)^n$ represents the probability of none of the chain links failing [58]. Using this weakest chain link premise, Weibull stated that if $1-P_n = e^{-n\varphi(x)}$ then all that is required to do is define a function $\varphi(x)$ [58]. Weibull's original CDF is shown in equation 4-8 [58]:

$$F(x) = 1 - e^{-(\frac{(x-\gamma)}{\eta})^{\beta}} \qquad \text{4-8}$$

Where γ represents a delay, or fail free time, η is a scale parameter (commonly referred to as characteristic life), β is the shape parameter, and x represents the time to failure. The Weibull distribution, due to its derivation, represents the failing distribution of the weakest links in a system [58, 59]. Time (x) may be revolutions of a bearing, strain, hours of operation, kilometers traveled, among others. Equation 4-8 represents the three parameter Weibull distribution and for this paper, the two parameter which removes the delay parameter from the CDF as shown in equation 4-9 was used to analyze failing strain at BGA corners.

$$F(x) = 1 - e^{-(\frac{x}{\eta})^{\beta}} \qquad \text{4-9}$$

Rearranging the CDF shown in equation 4-9 results in equation 4-10 as shown below and provides a method to linearize the Weibull distribution:

$$ln\left(ln\left(\frac{1}{1-F(x)}\right)\right) = \beta ln(x) - \beta ln(\eta) \qquad \text{4-10}$$

Before using the Weibull distribution, the following must be noted:

1. F(x) is the median rank (MR) of the position of a failure in the distribution.   MR is calculated by finding the most likely position of the failure by setting the cumulative binomial distribution equal to 0.50 and solving for MR [60].

2. This method for ranking the failures automatically ensures some correlation since failures are ordered from shortest to longest time to failure.   Because of this, higher correlation values are required for Weibull.

3. Although there is no mathematical derivation proving the applicability of the Weibull distribution, it is widely used because it works well, especially in life data analysis [61].

For the Weibull analysis of failing and surviving strains, the suspensions were accounted for when calculating median rank position in the distribution.   Whether or not to include suspensions is sometimes debated, but this author sides with those who believe that the suspensions are part of the total population and to not account for them results in the characteristic life (η) being underestimated.   Rank Regression on the x-axis (RRX) was used with Type I (time) confidence bounds.

Figure 45 shows the probability plots (strain vs. unreliability) of all PCB laminates. The probability plot shows the Weibull distribution is a good fit for the failure data. For linear regression, the correlation coefficient (ρ) shows the strength of a relationship between two variables and ranges in value from -1 to 1. The closer ρ is to -1 or 1, the stronger the relation.
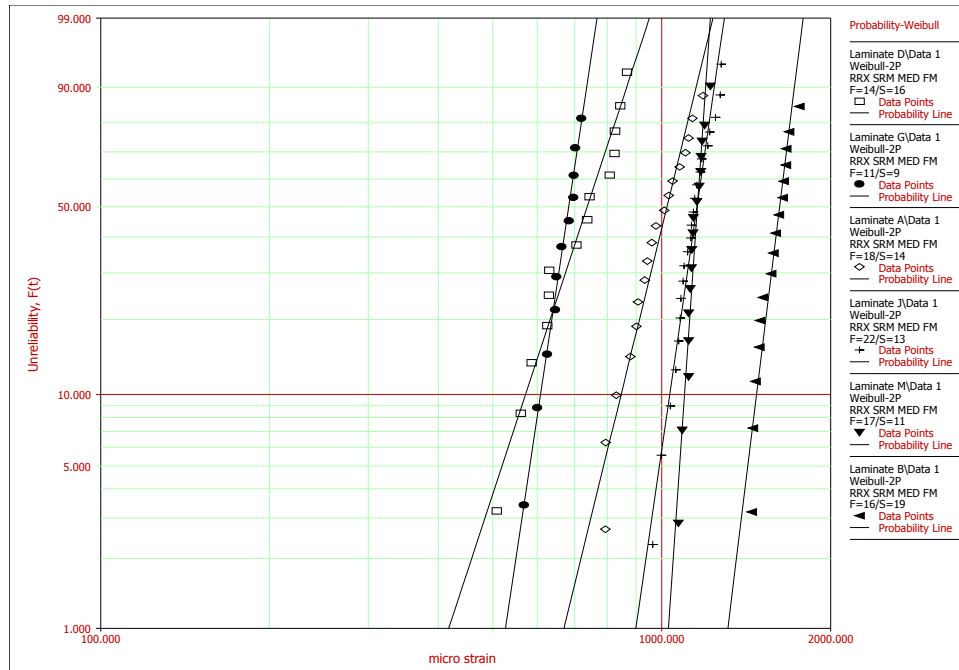
Figure 45: Probability Plot of All PCB Laminates

For Weibull analysis, ρ indicates the strength of the relationship between the median ranks and the failure data. Table 6 shows the ρ values for all PCB laminates with the minimum ρ value being 0.9625, which indicates the Weibull distribution is a good fit for the data.

Table 6: Correlation Coefficients for Weibull Distribution (all PCB laminates)

Laminate	A	B	D	M	G	J
rho (ρ)	0.9776	0.9625	0.9827	0.9667	0.9948	0.9831

Since there are two parameters, **β** and **η**, in the Weibull distribution, confidence intervals are a function of these two parameters. The contour plot is used to represent the confidence intervals of **β** and **η** and the contour plot for all six PCB laminates is shown in Figure 46 to 90% CI. As the figure shows, PCB laminate B has a much higher **η** value than the other laminates. The **η** values represent the 62.3% failure of the population and should correlate well to a PCB laminate's resistance to pad-crater.

54
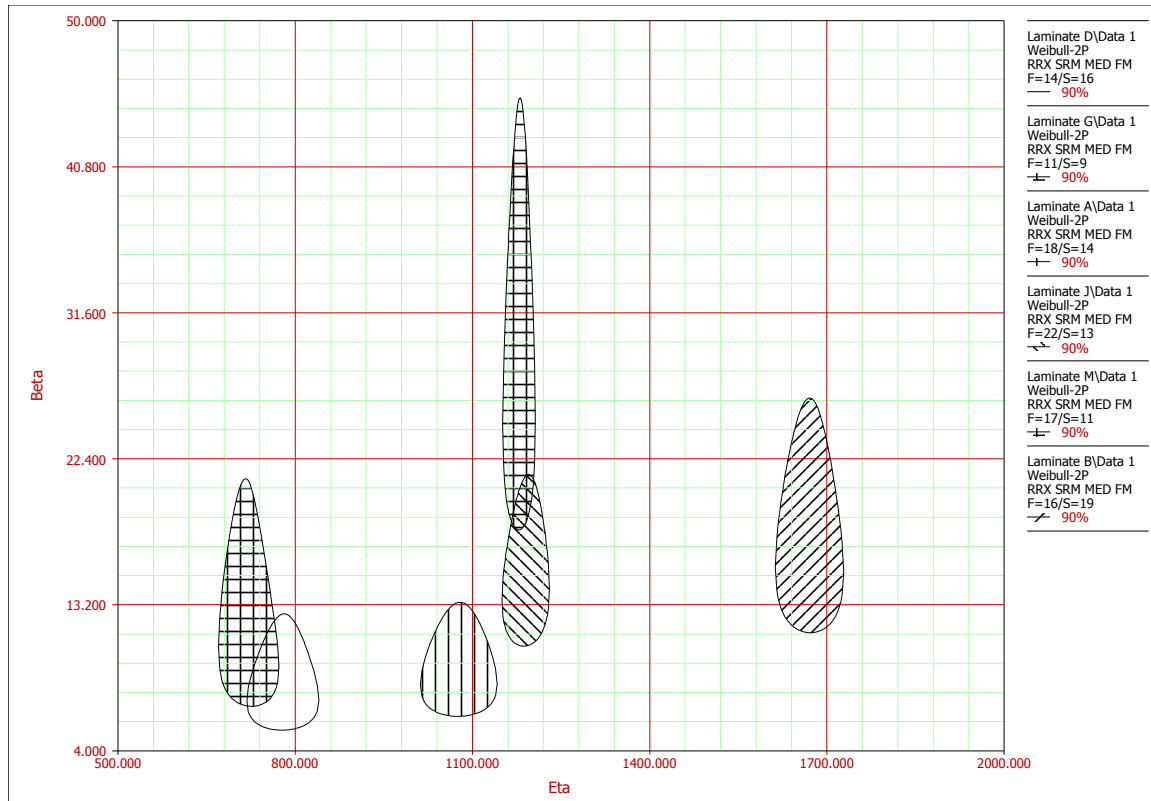
Figure 46: Contour Plot, Eta vs. Beta for all PCB laminates

Of more interest are the BX% lives, where X represents the percentage failed population for a given **β** and **η** value. Table 7 shows the B0.1 lives for all laminates, and Figure 47 shows a graphical representation of Table 7. As can be seen from Figure 47, PCB laminate B is still the best performer, but at lower strain levels the difference is much smaller.

Table 7: B0.1 Strain Lives (µε) of laminates and correlation coefficient with suspensions with 90% CIs

	B0.1		
Laminate	**Lower**	**Nominal**	**Upper**
D	227	306	413
G	394	457	530
A	438	533	649
J	592	685	792
M	906	963	1024
B	1050	1168	1299

55
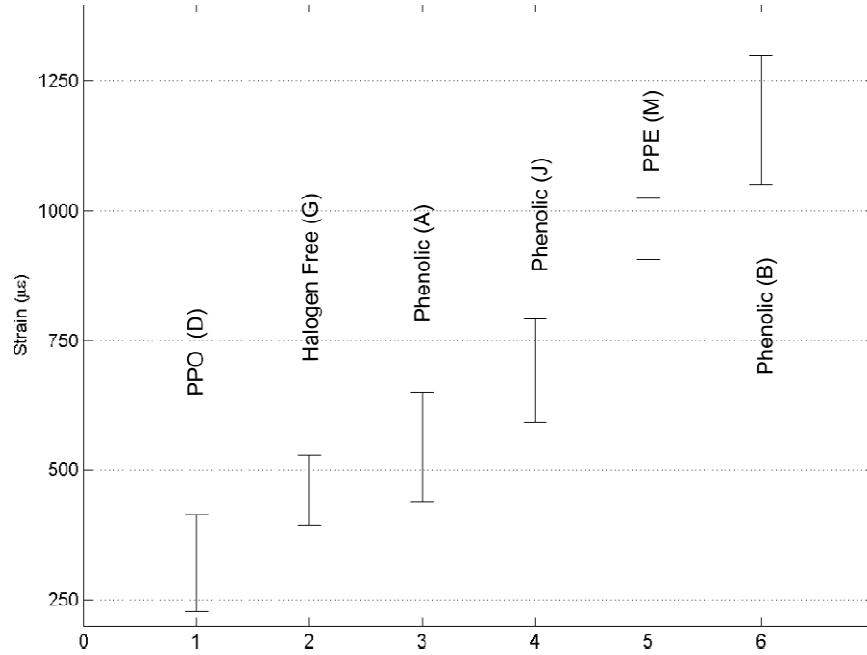
Figure 47: Weibull B0.1 (90% CI) for all laminates

4.2.6 PCBA Strain Energy

The energy to displace the PCBA is calculated using equation 4-11, where F is applied force by the load transducer, and d is the displacement of the PCBA as measured by independent linear variable displacement transducer (LVDT).

$$Energy_{t+1} = \frac{(F_{t+1} + F_t)}{2}(d_{t+1} - d_t)$$

4-11

The strain energy of deflection is the sum of all the energy terms from equation 4-11 as shown in equation 4-12.

$$Strain\ Energy = \sum_{t=1}^{n} Energy_t$$

4-12

Figure 48 shows the strain energy vs. deflection for bare PCB laminate A and B, and PCBA for one test of each laminate. Laminate B and A's E values were measured to be 21.53 and 23.68 GPa respectively, and their nominal B0.1 lives were 1168 µε and 533

56

με respectively. As can be seen from the plot, the laminate with the higher E value requires more energy to displace.
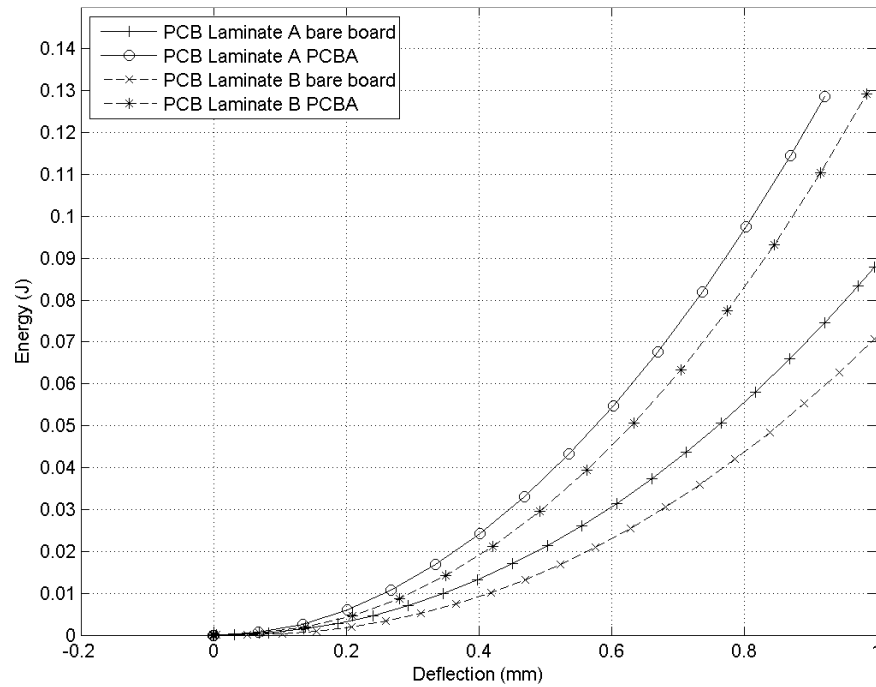
Figure 48: Strain energy of bare PCB and PCBA displacement, Laminate A & B

A comparison of difference in strain energy with and without BGA component for laminate A and B is shown in Figure 49. As can be seen in Figure 49, the additional stiffness the presence of the BGA adds to the two PCBs with different E values is almost identical. This suggests that the strain energy is driven primarily by the area outside of the BGA shadow.
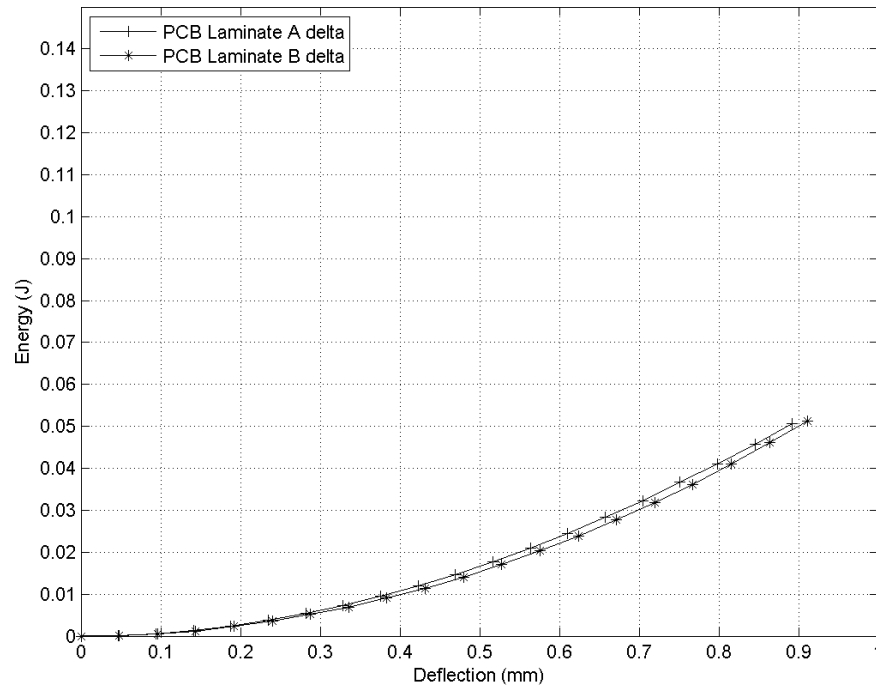
Figure 49: Difference in strain energy of displacement for PCBA and bare PCB, Laminate A & B

4.3 Micro-Indentation Hardness

4.3.1 Test Results

A sample micro-indentation is shown in Figure 50 and although the indentation may be difficult to see, when viewed through the microscope, the corners of the indentation are easily determined. Statistical analysis of all micro-hardness showed that the three parameter Weibull distribution was the best fitting across all the testing as determined by the correlation coefficient ρ. The β, η, γ, and ρ results for all hardness testing are shown in Table 8. The three parameter Weibull distribution may seem unlikely, but there are some underlying reasons it works well including the presence of filler in the resin and the undulation of the E-glass fabric weave which may affect results.

Figure 50: Laminate A, VH Indentation (VH = 32.2)

The three parameter Weibull probability plot of all hardness testing is shown in Figure 51 with the three most and least pad crater resistant laminates highlighted. As can be seen from the plot, the three parameter Weibull distribution fits the data well and the better performing laminates have lower **γ** values.

Table 8: Three Parameter Weibull Analysis of Hardness Testing

	A	B	D	M	G	J
β	1.87	2.15	2.23	2.70	5.10	1.03
η	8.65	3.56	9.07	8.52	16.14	5.77
γ	29.21	22.20	29.76	25.70	22.36	22.47
ρ	0.9902	0.9934	0.9912	0.9912	0.9933	0.9943
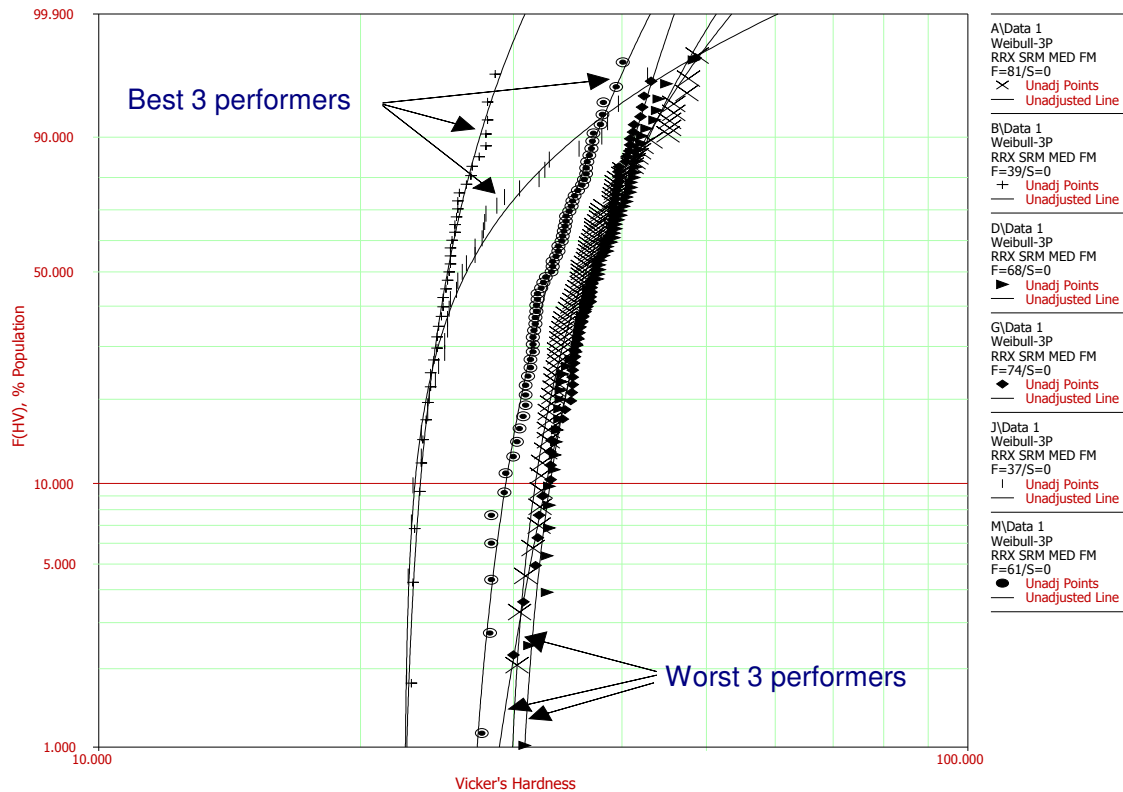
Figure 51: Three Parameter Weibull Probability Plot of Vicker's Hardness for all laminates

A\Data 1
Weibull-3P
RRX SRM MED FM
F=81/S=0
× Unadj Points
— Unadjusted Line

B\Data 1
Weibull-3P
RRX SRM MED FM
F=39/S=0
+ Unadj Points
— Unadjusted Line

D\Data 1
Weibull-3P
RRX SRM MED FM
F=68/S=0
► Unadj Points
— Unadjusted Line

G\Data 1
Weibull-3P
RRX SRM MED FM
F=74/S=0
◆ Unadj Points
— Unadjusted Line

J\Data 1
Weibull-3P
RRX SRM MED FM
F=37/S=0
| Unadj Points
— Unadjusted Line

M\Data 1
Weibull-3P
RRX SRM MED FM
F=61/S=0
● Unadj Points
— Unadjusted Line

4.3.2 Analysis

The filler in the laminates can be seen with scanning electron microscope (SEM) and

a sample image of Laminate B is shown in Figure 52.
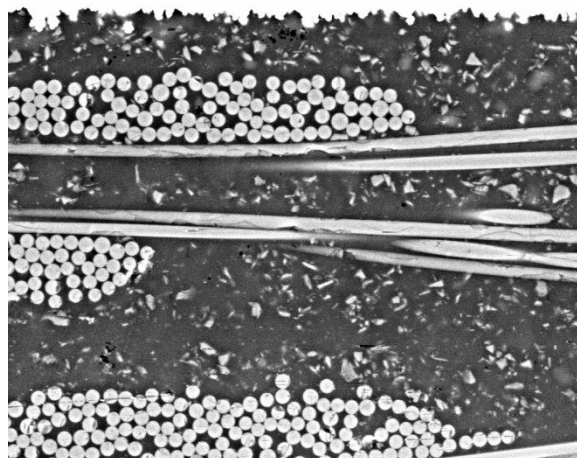
Figure 52: SEM image, PCB laminate B, 600x, 20 keV

The effect of ceramic fillers on the hardness measurements is unknown, but it is conceivable that if the Vicker's indentor pushed directly onto a ceramic particle, the measurement would be affected. All laminates had either values excluded from the measurements because they were outliers, or were bimodal. The reason for this is presently unknown, but given the undulation of the tows of the fabric weave, it is possible that the higher values are due to the VH indentor contacting the fabric weave resulting in artificially small indentation which results in higher hardness values. Figure 53 shows histogram plot of Laminate J with normal distribution overlaid.

Figure 53: Histogram of Sample 1, Laminate J

The cluster of measurements around 40 VH in Figure 53 illustrates that laminate J to be bimodal. The versatility of three parameter Weibull accommodates the bimodal nature of the VH measurements. The PDF plots of all laminates are shown in Figure 54. With the exception of laminate J, all PDFs are close to normal.

61
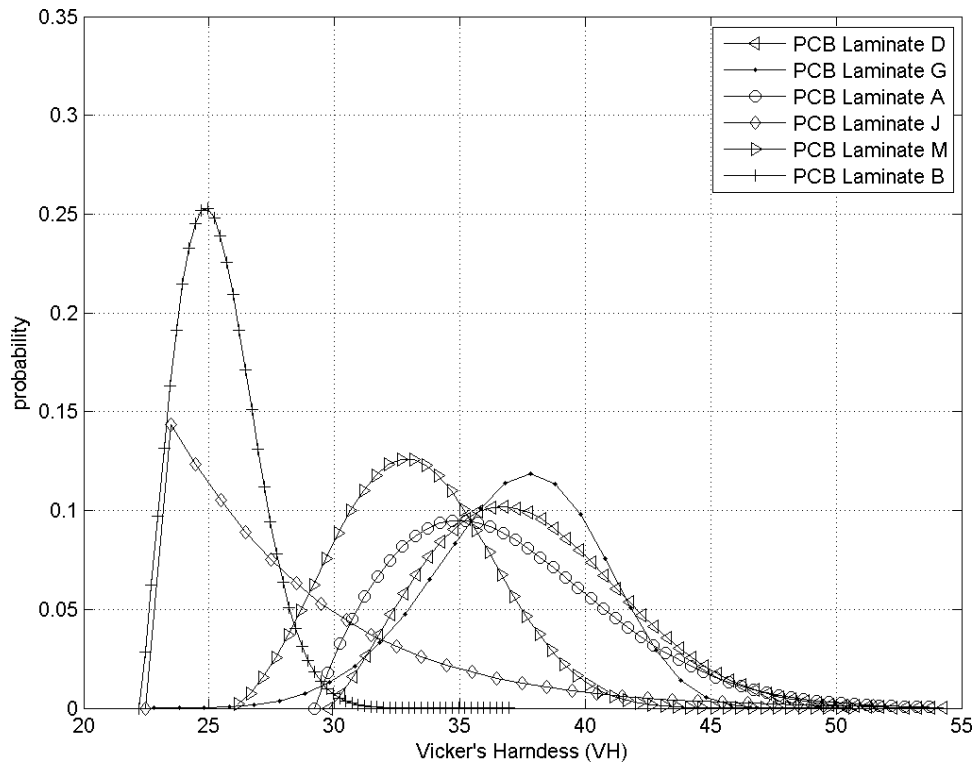
Figure 54: Three parameter Weibull PDF plots of all laminates

4.4 Tow a Measurements

4.4.1 Results

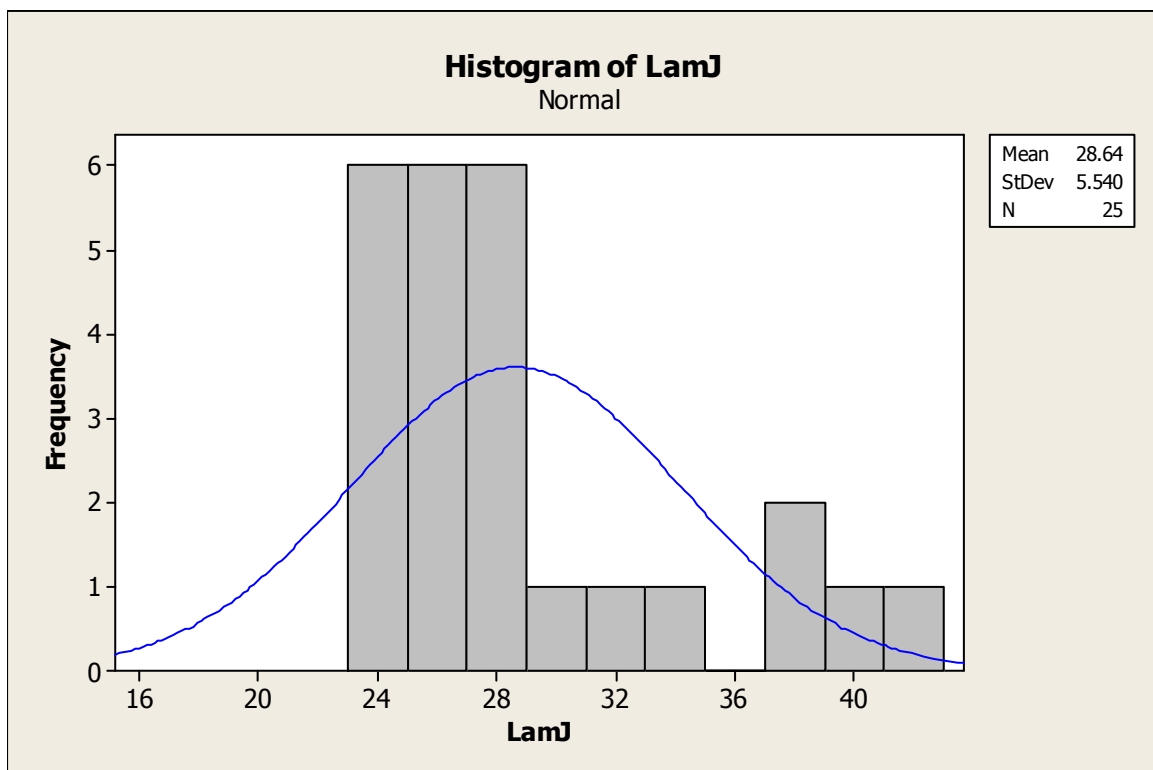The normal probability plots with 95% CIs of tow dimension *a* (see Figure 22) in both warp and fill direction are shown in Figure 55 and Figure 56 respectively. PCB laminate J is the most distinct from all test laminates because it has the smallest mean tow *a* dimension in both warp and fill direction at 132.1 μm and 250.1 μm respectively, and it is the third most resistant to pad crater. Comparison of the most and least pad-crater resistant laminates B and D shows there is no correlation to tow *a*. In the fill direction, laminate B and D have mean *a* values of 413.3 μm and 347.6 μm respectively. In the warp direction, laminate B and D have mean *a* values of 198.9 μm and 216.9μm respectively. Laminate B and D have larger tow *a* in both warp and fill directions than J, yet they represent the best and worst performers.

62
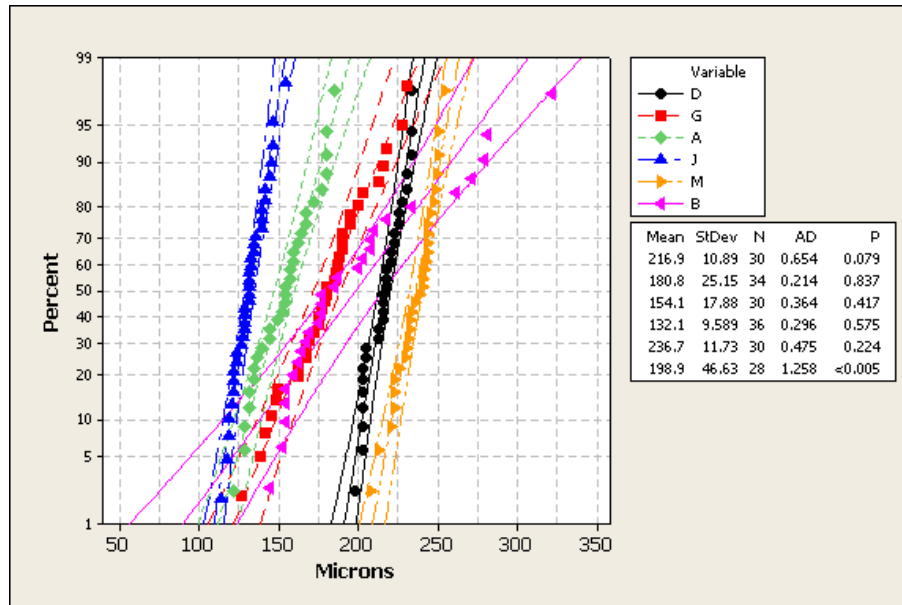
Figure 55: Tow Dimension *a*, warp Direction
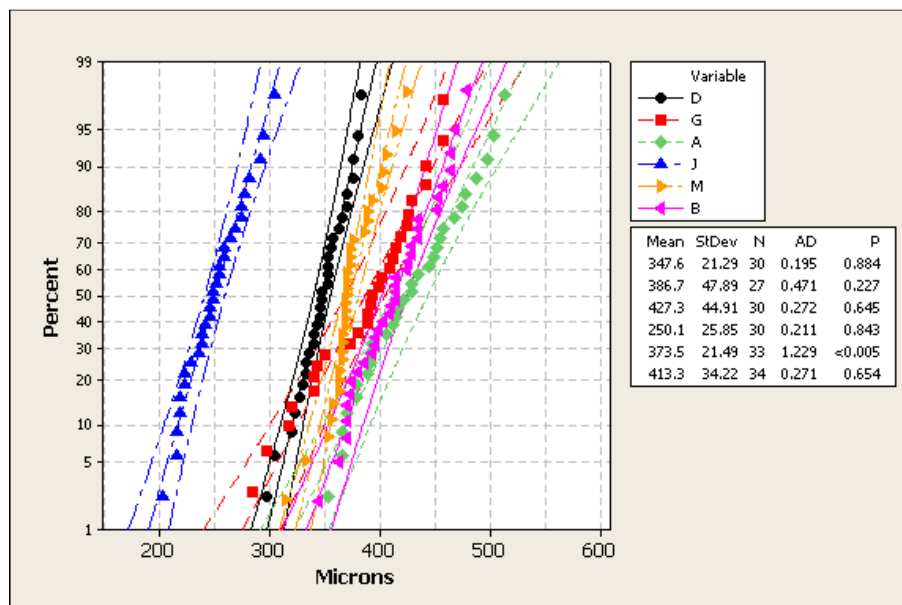
Figure 56:Tow Dimension *a*, fill Direction

Cross section images of laminate A and M under fluorescent light are shown in Figure 57. From the figures the difference in tow *a* dimensions in the warp direction can be easily seen.

PCB Laminate A   **PCB Laminate M**
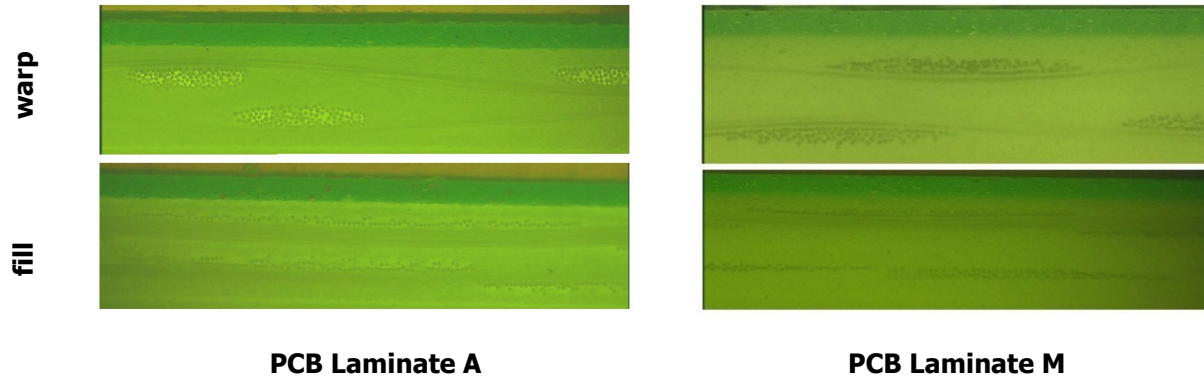
Figure 57: Cross sections of warp and fill directions, 100x magnification, fluorescent light.

4.4.2 Analysis

Laminate samples were polished with 1 µm grit to expose the top layer of weave. Figure 58 shows laminate M and as can be seen from the figure, the weave is continuous; that is to say, there are no openings in the weave.

fill direction

Figure 58: Laminate M weave, 50x magnification

Figure 59 shows the laminate J weave and highlights the area of the laminate where there is no E-glass weave. This discontinuous weave contributes to discontinuous properties at a microscopic level [38, 39]. Figure 60 shows a picture of a laminate J sample pad-crater and the opening in the weave where dye has penetrated is visible.

64
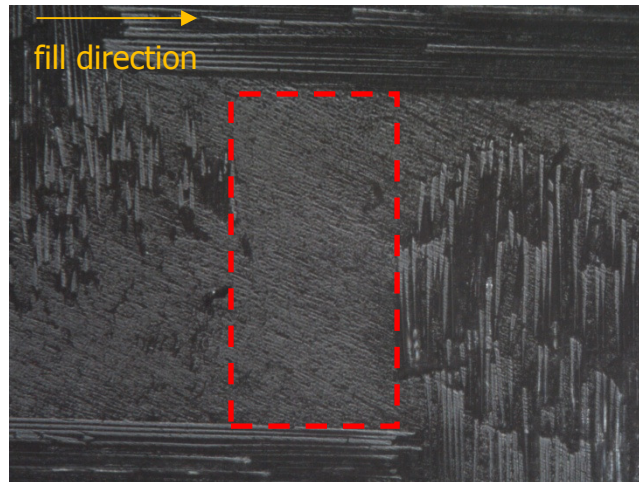
Figure 59: Laminate J weave, 50 x magnification
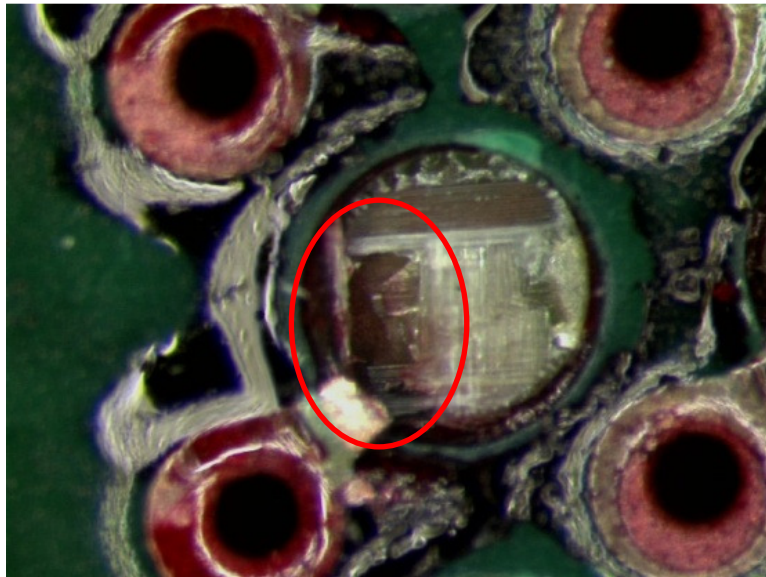
Figure 60: Laminate J Pad Crater, 27x magnification

4.5 Buttercoat thickness

4.5.1 Results and Analysis

Figure 61 shows the one standard deviation interval plot of all laminates in order of

least to most resistance to pad-crater from left to right. As the figure shows, there is

no relationship between buttercoat thickness and susceptibility to pad-crater. Laminate

J was the only laminate to have unspread glass as indicated by it having the lowest tow

a dimension in the fill and warp direction. Research has shown spread glass showed a

50% reduction in 1080 glass weave thickness as compared with unspread glass weave. [39]. The reduced thickness of E-glass weave should correlate into thicker buttercoat, or conversely, a thin buttercoat for unspread glass. This result is confirmed by PCB laminate J's thin buttercoat.
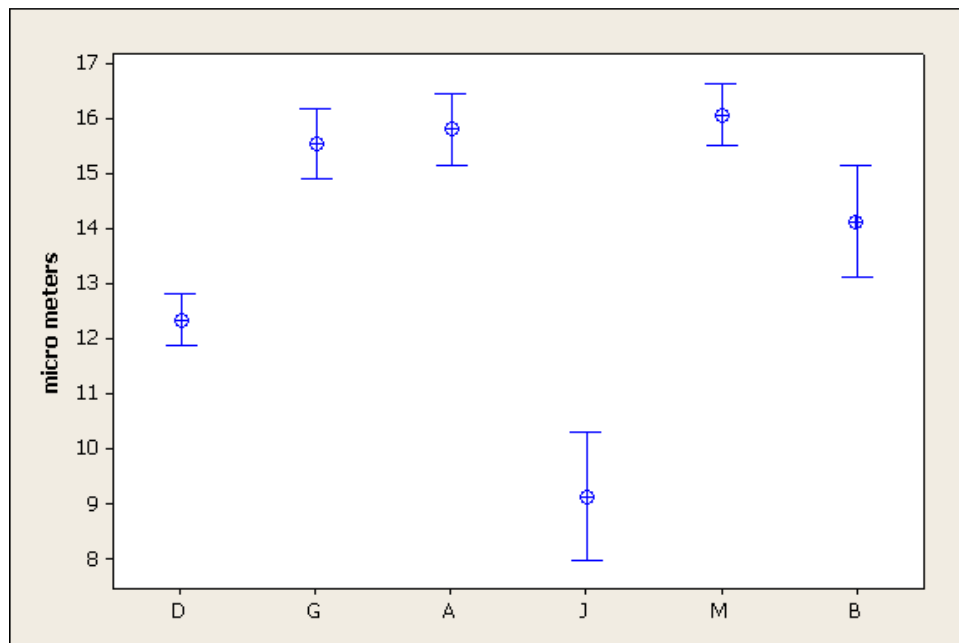
Figure 61: Buttercoat thickness interval plot to one sigma--All laminates

4.6 Correlation of Young's Modulus & VH to laminate susceptibility to Pad-Crater

This section presents linear regression analysis of all measurements made to susceptibility to pad crater.

4.6.1 Results and Analysis

Least squares regression analysis of mean E values for laminate only vs. **η** (B62.3%) VH values is shown in Figure 62. The correlation (ρ) between mean E and **η** VH is **0.636**, and R^2 is **40.5**% for the linear regression. Given that all the boards were made

66

from the same stack-up, the only variable between the laminates is the resin. This suggests mean E and **η** VH values are not necessarily correlated.
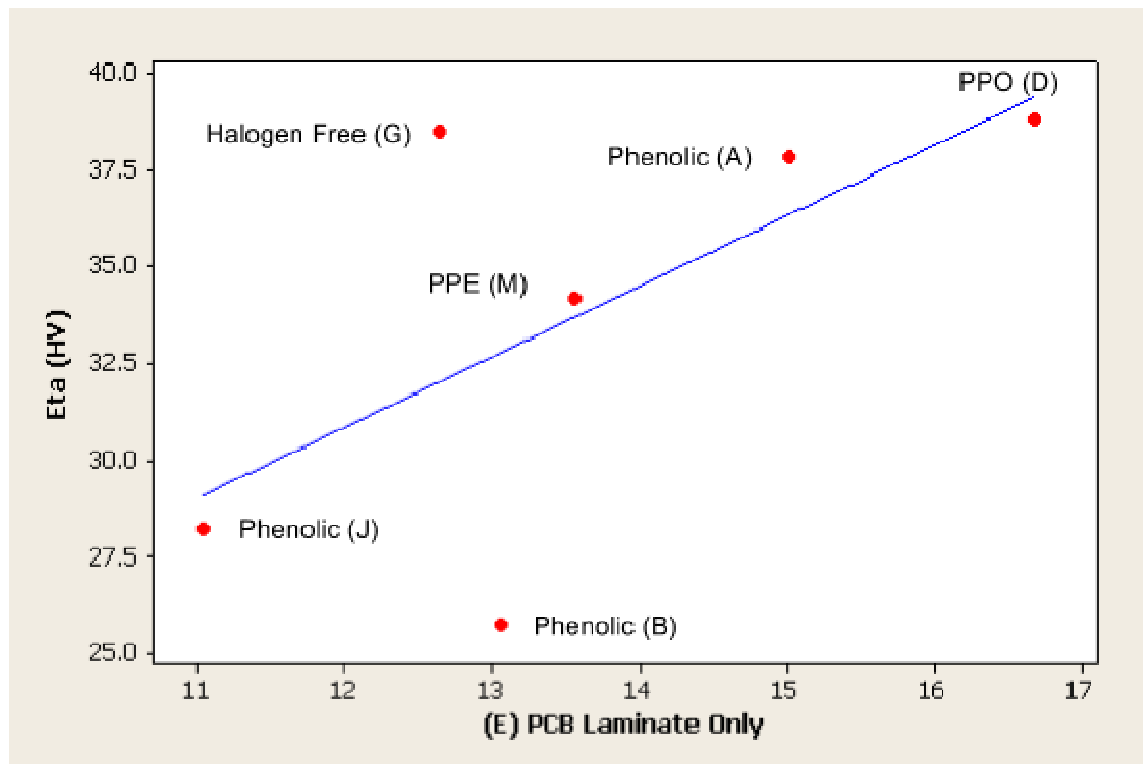
Figure 62: Scatter plot with regression of E vs. η (eta) VH

Figure 63 shows the scatter plot with least squares linear regression for nominal **η** (B62.3%) and B0.1% strain lives vs. **η** (B62.3%) VH for each PCB laminate. The ρ is -0.885 and the R^2 is 72.9% for nominal strain **η** vs. VH **η**. For B0.1% strain lives vs. **η** VH, the R^2 is 55.2% and ρ is -0.801. Clearly the relationship between **η** strain lives vs. VH **η** is better. The inverse relation **η** strain lives and VH **η** suggests that decreasing the VH of the buttercoat translates as less susceptibility to pad-crater under monotonic spherical bend.
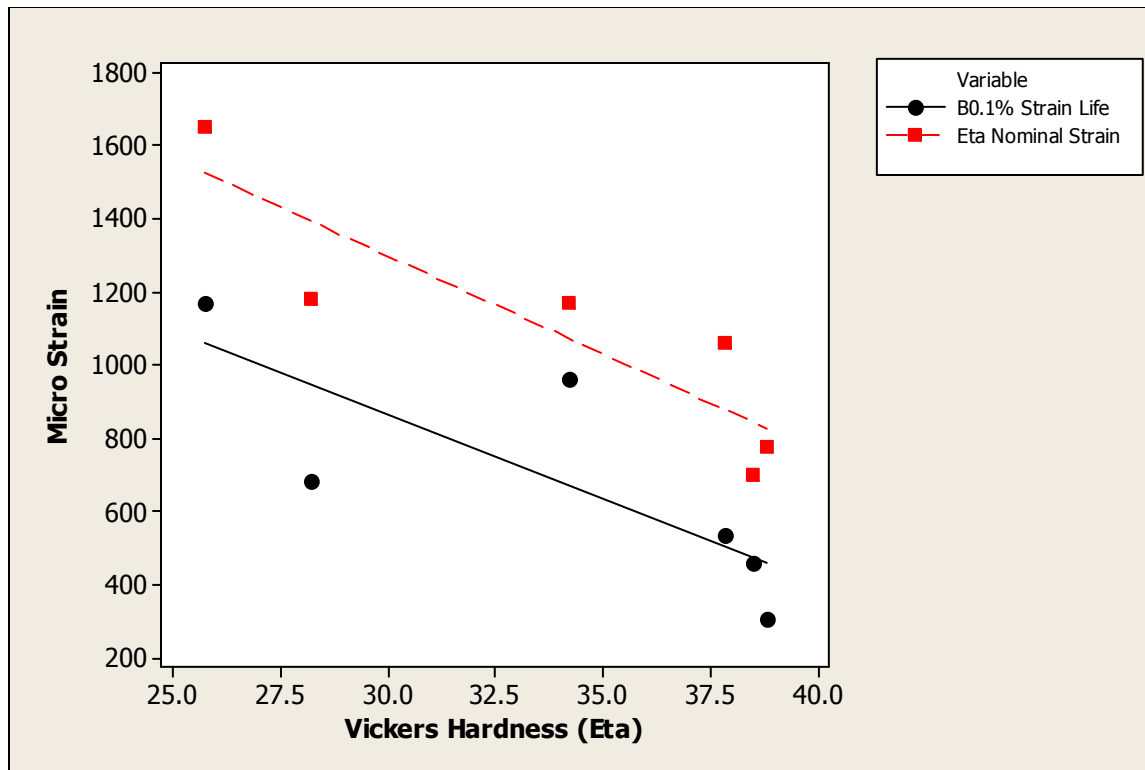
Figure 63: Scatterplot nominal η (eta) & B0.1% strain lives vs. η (eta) VH

Chapter 5: Conclusions

Pad-crater has been an unintended consequence of an environmental initiative which has made critical the understanding of base material properties and their susceptibility to pad-crater. It has also necessitated a better fundamental understanding of a PCB laminate's response to spherical bend.

For the materials studied:

- There is no correlation between Young's Modulus (E) and susceptibility to pad-crater.

- Comparison of με / mm of deflection slopes under spherical bend showed an inverse relationship between PCB mean laminate E and slope values.

- Spherical bend of pure laminate as per IPC/JEDEC 9707 [23] cannot be idealized as a point load on a simple circularly supported plate with the assumption of isotropic material properties. Test results showed the orthotropic nature of the laminate affects the strain response.

- Spherical bend of bare PCB as per IPC/JEDEC 9707 [23] cannot be idealized as a point load on a simply circularly supported plate. Measurements inside and outside the BGA shadow area show material and geometric non-linearities at work. The weakened area of the BGA shadow must be accounted for when modeling.

- There were no electrical opens on any PCBA spherical bend test confirming that pad-crater precedes electrical failure.

- When PCB surface strains at a BGA corner are assumed to indicate solder joint strains under spherical bend, the two parameter Weibull distribution fits the failure data well.

- Comparison of strain energy for bare PCB and PCBA subjected to spherical bend showed the additional stiffness a BGA adds to a PCB is almost identical when comparing two laminates of different E values. Put another way, strain energy is driven primarily by the PCB area outside the BGA shadow.

- Three parameter Weibull distribution is the best distribution for Vicker's hardness values of PCB laminate resin (buttercoat).

- There is no correlation between laminate susceptibility to pad-crater and tow a dimension or buttercoat thickness. Laminate J, the coarsest E-glass weave, showed that pad-crater can travel through openings in the weave.

- Spread glass weaves result in thicker buttercoat.

- The R^2 values for least squares linear regression of **η** (B62.3%) VH vs. mean E equaled 40.5%.   The correlation ρ between these same variables was 0.636. The low R^2 suggests there is insufficient evidence of a linear relationship between **η** VH and mean E.

- Linear regression of **η** (B62.3%) strain lives vs. **η** (B62.3%) VH had a ρ of -0.885 and R^2 of 72.9%.   Linear regression of B0.1% strain lives vs. **η** VH had R^2 of 55.2% and ρ = -0.801.   The relationship between **η** strain lives and **η** VH is better and suggests reducing the hardness of the resin increases a PCB laminate's resistance to pad-crater.

References

[1] J. Fjelstad and T. Stefano, "Where Are We Headed," *Electronic Packaging and Production* (December 1999): 16-20.

[2] Clyde F. Coombs, Jr., and editor-in-chief, *Printed Circuits Handbook*, 6th ed. (New York: McGraw-Hill Professional, 2008), 45.7

[3]Clyde F. Coombs, Jr., and editor-in-chief, *Printed Circuits Handbook*, 6th ed. (New York: McGraw-Hill Professional, 2008), 7.7-7.8

[4]Clyde F. Coombs, Jr., and editor-in-chief, *Printed Circuits Handbook*, 6th ed. (New York: McGraw-Hill Professional, 2008), 7.17

[5]Clyde F. Coombs, Jr., and editor-in-chief, *Printed Circuits Handbook*, 6th ed. (New York: McGraw-Hill Professional, 2008), 7.4

[6] IPC/JEDEC 9702, Monotonic Bend Characterization of Board-Level Interconnects, June 2004

[7]Mukadam, Muffadal et al. 2005. "Impact of cracking beneath solder pad in printed circuit boards on reliability of ball grid array packages." Surface Mount Technology International, Rosemont, IL. September 25

[8]Turbini, Laura. 2007. Processing and material issues and related lead-free soldering. Journal of Materials Science: Materials in Electronics 18: 147-54.

[9]Gray, Brian and J. McMahon. 2011. Material Testing and Mitigation Techniques for Pad-Crater Defects. *Journal of Surface Mount Technology* 24, no. 4 (October 30): 33-38

[10]G., Godbole et al. 2009. On the nature of pad cratering. Electronic Comonents and Technology Conference, San Diego, CA. 26-29 May

[11]Jones, F. 1989. Role of moisture diffusions and matrix plasticization on environmental stress corrosion of GRP. *The Journal of Strain and Analysis of Engineering Design* 24, no. 4: 223-233.

[12]Gaur, U, and B Miller. 1990. Effects of environmental exposure on fiber epoxy interfacial shear strength. Journal of polymer composites 11, no. 4: 217-22.

[13]Brown, E, A Davis, K Jonnalagadda, and N Sottos. 2005. Effect of surface treatment on the hydrolytic stability of E-glass fiber bundle tensile strength. *Composites Science and Technology* 65, no. 1: 129-36.

[14] Gray, Brian and J. McMahon. 2010. Mechanical Failures in Pb-free Processing: Selected Mitigation Techniques for Pad Crater Defects. Paper presented at Surface Mount Technology Association International, Orlando, FL. October 24

[15]Nadimpalli, Siva and J. Spelt. 2010. A Geometry and Size Independent Failure Criterion for Fracture Prediction in Lead-Free Solder Joints. Paper presented at the International Conference on Soldering and Reliability, Toronto, ON. May 17..

[16]Nadimpalli, Siva and J. Spelt. 2011. Characterization and Prediction of Pad-Crater Fracture in Lead-Free Compatible PCBs. Paper presented at International Conference on Soldering Reliability, Toronto, ON. May 4

[17] McMahon, John, and Brian Gray. 2011. Laminate Resistance to Pad Crater Defects: Comparative Spherical Bend Testing. *Journal of Surface Mount Technology* 24, no. 3 (30 July): 25-32

[18] Zaal, J, H Hochstenbach, W Driel, and G Zhang. 2008. An Alternative Solder Interconnect Reliability Test to Evaluate Drop Impact Performance. *Electronic Components and Technology Conference* (May): 1181-86

[19] Ahmad, Mudasir, Jennifer Burlingame, and Cherif Guiguis. 2009. Comprehensive Methodology to Charaterize and Mitigate Pad Cratering in Printed Circuit Boards. Journal of Surface Mount Technology 22, no. 1: 21-28.

[20] Roggeman, Brian, Peter Borgeson, Jing Li, Guarav Godbole, Pushkraj Tumne, K Srihari, Tim Levo, and James Pitaressi. 2008. Assessment of PCB Pad Cratering Resistance by Joint Level Testing. *Electronic Components and Technology* (May): 884-92.

[21] Zhao, X, J Caers, J de Vries, E Wong, and R Rajoo. 2007. A Component Level Test Method for Evaluating the Resistance of Pb-free BGA Solder Joints to Brittle Fracture under Shock Impact. *Electronic Components and Technology*: 1523-29.

[22]Cai, M, D Xie, Z Zhang, Billy Hu, X Su, Y Tao, and B Yu. 2010. Investigation on PCB Pad Strength. *Electronic Components and Technology*: 1226-29.

[23] IPC/JEDEC-9707, Spherical Bend Test Method for Characterization of Board Level Interconnect

[24] Towashiraporn, P, P Crosbie, and Y Lee. 2008. The Effect of PCB Flexural Modes on Dynamic Reliability of Ball Grid Array Packages. *tronic Components and Technology* (May): 1804-11.

[25] Hsieh, G, and A McAllister. 2005. Flip Chip Grid Array Component Testing under Board Flexure. *Electronic Components and Technology* (May): 937-44.

[26] Mercado, Lei, George Hsieh, and Steven Girouard. 2006. Electronic Packaging Solder Joint Reliability Assessment with a Mechanics Based Strain Gage Methodology. *IEEE Transactions on Components and Packaging Technologies* 29, no. 1 (March): 5-12.

[27] Mercado, Lei, Steven Girouard, and George Hsieh. 2004. A Mechanics-Based Strain Gage Methodology for Solder Joint Reliability Assessment. *International Conference on Thermal and Mechanical Simulation and Experiments in Micro-electronics and Micro-Systems*: 533-41.

[28] Ready, W, L Turbini, and S Stock. 1996. Conductive Anodic Filament Enhancement in the Presence of a Polyglycol - Containing Flux. *Reliability Physics Symposium*: 267-73.

[29] Roggeman, B. 2009. Characterizing the Lead-Free impact on PCB Pad Craters. Paper presented at APEX 2010, BANNOCKBURN, IL. November.

[30] Peng, Y, and Q Xiaolong. 2005. "The influence of curing systems on epoxide based PCB laminate performance". *Circuit World*

[31] Wagner, W, and A Pruss. 1993. International Equations for the Saturation Properties of Ordinary Water Substance. *Journal of Physical Chemistry* 22, no. 3: 783-87.

[32] Clyde F. Coombs, Jr., and editor-in-chief, *Printed Circuits Handbook*, 6th ed. (New York: McGraw-Hill Professional, 2008), 7.17

[33] Clyde F. Coombs, Jr., and editor-in-chief, *Printed Circuits Handbook*, 6th ed. (New York: McGraw-Hill Professional, 2008), 7.2

[34] Clyde F. Coombs, Jr., and editor-in-chief, *Printed Circuits Handbook*, 6th ed. (New York: McGraw-Hill Professional, 2008), 7.4

[35] Clyde F. Coombs, Jr., and editor-in-chief, *Printed Circuits Handbook*, 6th ed. (New York: McGraw-Hill Professional, 2008), 7.6

[36] Clyde F. Coombs, Jr., and editor-in-chief, *Printed Circuits Handbook*, 6th ed. (New York: McGraw-Hill Professional, 2008), 7.9-7.10

[37] Sanapala, R. (2008), "Characterization of FR-4 Printed Circuit Board Laminates Before and After Exposure to Lead-Free Soldering Conditions", Unpublished master's thesis, University of Maryland, College Park, Maryland, USA. pp. 9

[38] Dudek, R. 2009. "Opening Eyes on Fiber Weave and CAF". Paper presented at IPC APEX EXPO, Bannockburn, IL. April 14.

[39] Dudek, R, and P Goldman. Year. Advanced Glass Reinforcement Technology for Improved Signal Integrity. *Printed Circuit Board Design and Fab*, Publication Date. http://pcdandf.com/cms/magazine/212/4238-advanced-glass-reinforcement-technology-for-improved-signal-integrity (accessed March 13, 2012).

[40] Clyde F. Coombs, Jr., and editor-in-chief, *Printed Circuits Handbook*, 6th ed. (New York: McGraw-Hill Professional, 2008), 7.15

[41] Sn-Ag-Cu Properties and Creep Data. NIST.

http://www.metallurgy.nist.gov/solder/clech/Sn-Ag-Cu_Other.htm#Young (accessed

January 14, 2012).

[42] Bradley, Edwin, Carol A. Handwerker, Jasbir Bath, Richard D. Parker, and Ronald

W. Gedney. 2007. Review and Analysis of Lead-Free Solder Material Properties. In

Lead-free electronics: iNEMI projects lead to successful manufacturing, 100. Hoboken,

N. J.: Wiley-IEEE Press.

[43] Basaran, Cemal, and Jianbin Jiang. 2002. Measuring intrinsic elastic modulus of

Pb/Sn solder alloys. *Mechanics of Materials* 34 (15 April): 349-62.

[44] Siviour, C. R., S. M. Walley, W. G. Proud, and J. E. Field. 2005. Mechanical

properties of SnPb and lead-free solders at high rates of strain. *Journal of Physics D:*

Applied Physics 38 (November): 4131-39.

[45] Fan, Xuejun, Min Pei, and Pardeep Bhatti. 2006. Effect of Finite Element Modeling

Techniques on Solder Joint Fatigue Life Prediction of Flip-Chip BGA Packages. *Electronic*

Components and Technology (June): 972-80.

[46] Ding-Siang Wang, Jenn-Ming Song, Shi-Ching Lin. 2010. Title. Mechanical

Properties of Electrodeposited copper foils in PCB applications, Taipei, Taiwan. 20-22

October.

47 McCaslin, Luke, and Suresh Sitaraman. 2008. Methodology for Modeling Substrate

Warpage Using Copper Trace Pattern Implementation. *Electronic Components and*

Technology (May): 1582-86.

[48]Clyde F. Coombs, Jr., and editor-in-chief, *Printed Circuits Handbook*, 6th ed. (New York: McGraw-Hill Professional, 2008), 6.16

[49] IPC/JEDEC 9704 Printed Wiring Board Strain Gage Test Guideline

[50] Perry, C. C. 1989. Data-Reduction Algorithms for Strain-Gage Rosette Measurements. *Experimental Techniques* (May): 13-18.

[51] D638-10 Standard Test Method for Tensile Properties of Plastics, American Society for Testing and Materials, 2010

[52] Standard Test Method for Knoop and Vickers Hardness of Materials, American Society for Testing and Materials, 2010

[53] IPC-TM-650 2.2.2B, Optical Dimensional Verification

[54] Ferdinand P. Beer, E. Russell Johnston, "Mechanics of Materials, Second Edition", (McGraw-Hill Book Company Europe, 1992), 60.

[55] Stephen W. Tsai and H. Thomas Hahn, *Introduction to Composite Materials* (Westport, Conn.: Technomic Publishing Co, Inc., 1980), 69

[56] Ansel C. Ugural, *Stresses in Beams, Plates, and Shells*, 3rd ed. (Boca Raton: CRC Press, 2009), 143

[57] E. Russell Johnston Ferdinand P. Beer, *Mechanics of Materials* (London: McGraw-Hill Publishing Co., 1992), 386

[58] Weibull, Waloddi. 1951. A Statistical Distribution Function of Wide Applicability. *ASME Journal of Applied Mechanics* (September): 293-97

[59] Dimitri Kececioglu, *Reliability Engineering Handbook* (Englewood Cliffs, N.J.: Prentice Hall, 1991), 313

[60] Dimitri Kececioglu, *Reliability Engineering Handbook* (Englewood Cliffs, N.J.: Prentice Hall, 1991), 283

[61] Abernethy, Robert B. 2000. *The New Weibull Handbook,Fourth Edition, Subtitle, Reliability & Statistical Analysis for Predicting Life, Safety, Survivability, Risk, Cost and Warranty Claims*. 4th ed. publication place: Robert B Abernethy., 33